

1 **A genetically encoded red fluorescence dopamine biosensor enables dual imaging of**
2 **dopamine and norepinephrine**

3
4
5 Chihiro Nakamoto^{a,b,1}, Yuhei Goto^{c,d,e,1}, Yoko Tomizawa^{c,d}, Yuko Fukata^{f,g}, Masaki Fukata^{f,g}, Kasper
6 Harpsøe^h, David E. Gloriam^h, Kazuhiro Aoki,^{c,d,e,2} and Tomonori Takeuchi^{a,b,2}

7
8 ^aDepartment of Biomedicine, Aarhus University, Hoegh-Guldbergsgade 10, DK8000, Aarhus C,
9 Denmark

10 ^bDanish Research Institute of Translational Neuroscience - DANDRITE, Nordic-EMBL Partnership for
11 Molecular Medicine, Aarhus University, Hoegh-Guldbergsgade 10, DK8000, Aarhus C, Denmark

12 ^cQuantitative Biology Research Group, Exploratory Research Center on Life and Living Systems
13 (ExCELLS), National Institutes of Natural Sciences, 5-1 Higashiyama, Myodaiji-cho, Okazaki, Aichi
14 444-8787, Japan

15 ^dDivision of Quantitative Biology, National Institute for Basic Biology, National Institutes of Natural
16 Sciences, 5-1 Higashiyama, Myodaiji-cho, Okazaki, Aichi 444-8787, Japan

17 ^eDepartment of Basic Biology, School of Life Science, SOKENDAI (The Graduate University for
18 Advanced Studies), 5-1 Higashiyama, Myodaiji-cho, Okazaki, Aichi 444-8787, Japan

19 ^fDivision of Membrane Physiology, Department of Molecular and Cellular Physiology, National
20 Institute for Physiological Sciences, National Institutes of Natural Sciences, 5-1 Higashiyama,
21 Myodaiji-cho, Okazaki, Aichi 444-8787, Japan

22 ^gDepartment of Physiological Sciences, School of Life Science, SOKENDAI (The Graduate University
23 for Advanced Studies), 5-1 Higashiyama, Myodaiji-cho, Okazaki, Aichi 444-8787, Japan

24 ^hDepartment of Drug Design and Pharmacology, University of Copenhagen, Universitetsparken 2,
25 2100 Copenhagen, Denmark

26

27 ¹These authors equally contributed to this work.

28 ²To whom correspondence may be addressed: Kazuhiro Aoki (k-aoki@nibb.ac.jp) and Tomonori

29 Takeuchi (tomonori.takeuchi@biomed.au.dk).

30

31 **Author ORCIDs**

32 Chihiro Nakamoto: <https://orcid.org/0000-0002-5685-8773>

33 Yuhei Goto: <https://orcid.org/0000-0002-5597-158X>

34 Yuko Fukata: <https://orcid.org/0000-0001-7724-8643>

35 Masaki Fukata: <https://orcid.org/0000-0001-5200-9806>

36 Kasper Harpsøe: <https://orcid.org/0000-0002-9326-9644>

37 David E. Gloriam: <https://orcid.org/0000-0002-4299-7561>

38 Kazuhiro Aoki: <https://orcid.org/0000-0001-7263-1555>

39 Tomonori Takeuchi: <https://orcid.org/0000-0002-9981-4260>

40

41 **Classification**

42 Major classification: Biological Sciences

43 Minor classification: Cell Biology

44

45 **Keywords**

46 GPCR | dopamine | norepinephrine | fluorescence probe | hippocampal neuron

47

48 **Author contributions**

49 Y.G., K.A. and T.T. designed research; C.N., Y.G., Y.T. and K.A. performed experiments; Y.F. and M.F.

50 supervised and prepared primary hippocampal neuron experiments; K.H. and D.E.G. performed *in silico*

51 structural analysis and suggested mutations; C.N., Y.G., and Y.T. analyzed the data; C.N., Y.G., K.A.
52 and T.T. wrote the manuscript.

53

54 The authors declare no competing interest.

55

56 **This PDF file includes:**

57 Main Text

58 Figures 1 to 5

59 **Abstract**

60 Dopamine (DA) and norepinephrine (NE) are pivotal neuromodulators that regulate a broad range of
61 brain functions, often in concert. Despite their physiological importance, untangling the relationship
62 between DA and NE in finely controlling output functions is currently challenging, primarily due to a
63 lack of techniques to visualize spatiotemporal dynamics with sufficiently high selectivity. Although
64 genetically encoded fluorescent biosensors have been developed to detect DA, their poor selectivity
65 prevents distinguishing DA from NE. Here, we report the development of a red fluorescent genetically
66 encoded GPCR (G protein-coupled receptor)-activation reporter for DA termed ‘R-GenGAR-DA’. More
67 specifically, a circular permuted red fluorescent protein (cpmApple) was inserted into the third
68 intracellular loop of human DA receptor D1 (DRD1) followed by the screening of mutants within the
69 linkers between DRD1 and cpmApple. We developed two variants: R-GenGAR-DA1.1, which
70 brightened following DA stimulation, and R-GenGAR-DA1.2, which dimmed. R-GenGAR-DA1.2
71 demonstrated reasonable dynamic range ($\Delta F/F_0 = -50\%$) and DA affinity ($EC_{50} = 0.7 \mu M$) as well as the
72 highest selectivity for DA over NE (143-fold) amongst available DA biosensors. Due to its high
73 selectivity, R-GenGAR-DA1.2 allowed dual-color fluorescence live imaging for monitoring DA and NE,
74 combined with the existing green-NE biosensor GRABNE1m, which has high selectivity for NE over
75 DA (>350-fold) in HeLa cells and hippocampal neurons grown from primary culture. By enabling precise
76 measurement of DA, as well as simultaneous visualization of DA and NE, the red-DA biosensor R-
77 GenGAR-DA1.2 is promising in advancing our understanding of the interplay between DA and NE in
78 organizing key brain functions.

79 **Significance Statement**

80 The neuromodulators dopamine and norepinephrine modulate a broad range of brain functions, often in
81 concert. One current challenge is to measure dopamine and norepinephrine dynamics simultaneously
82 with high spatial and temporal resolution. We therefore developed a red-dopamine biosensor that has
83 143-fold higher selectivity for dopamine over norepinephrine. Taking advantage of its high selectivity
84 for dopamine over norepinephrine, this red-dopamine biosensor allowed dual-color fluorescence live
85 imaging for monitoring dopamine and norepinephrine in both HeLa cells and hippocampal neurons *in*
86 *vitro* combined with the existing green-norepinephrine biosensor that has 350-fold selectivity for
87 norepinephrine over dopamine. Thus, this approach can provide new opportunities to advance our
88 understanding of high spatial and temporal dynamics of dopamine and norepinephrine in normal and
89 abnormal brain functions.

90 **Introduction**

91 The catecholaminergic neuromodulators dopamine (DA) and norepinephrine (NE) have very high
92 structural similarity, differing only by a single hydroxy group. Dopaminergic projections mainly
93 originate from the ventral tegmental area and substantia nigra pars compacta (1), whilst noradrenergic
94 projections originate from the locus coeruleus (LC) (2, 3). It was discovered recently that noradrenergic
95 LC axons co-released DA along with NE (4–6). DA is involved in reward (7, 8), motivation (9), novelty
96 response (10), and motor control (11, 12). In addition, the involvement of DA and NA in many brain
97 functions overlaps (13, 14), such as learning and memory (10, 15), arousal (16, 17), and stress response
98 (6, 18). In particular, the prefrontal cortex receives both dopaminergic and noradrenergic projections,
99 and these systems are involved in attention (19, 20) and working memory (21–23). Furthermore,
100 dysfunction of dopaminergic or noradrenergic systems are thought to be associated with psychiatric
101 disorders and neurodegenerative diseases, such as attention-deficit/hyperactivity disorder (ADHD),
102 schizophrenia, and Parkinson’s disease (24–26).

103 Although interactions between dopamine and norepinephrine theoretically depend on the timing of
104 release, spatial diffusions, concentrations, and neuromodulator ratios, little is actually known about these
105 properties with high spatial and temporal resolution within the same preparation due to the technical
106 limitations. For example, microdialysis with high-performance liquid chromatography has high
107 sensitivity and selectivity to detect either DA and NE, but suffers from poor spatial and temporal
108 resolution (27, 28). In contrast, fast-scan cyclic voltammetry (29) and a synthetic catecholamine
109 nanosensor (30) have higher sensitivity and temporal resolution, but cannot distinguish between DA and
110 NE. A method combining sensitivity, specificity, and spatiotemporal resolution is required to
111 satisfactorily answer research questions regarding timing of release, spatial diffusions, concentrations,
112 and ratios.

113 Recently developed genetically encoded fluorescent biosensors are able to detect extracellular DA
114 or NE with high spatial and temporal resolution and sensitivity in freely moving animals using *in vivo*

115 imaging (31–34). Binding of DA or NE to the sensor induces a conformational change, which couples
116 with a change in the fluorescence of circular-permutated fluorescent protein, such as green fluorescent
117 protein (GFP) for green fluorescence (31–34) and mApple for red fluorescence (34). The green-NE
118 biosensor, GRAB_{NE1m} (abbreviated NE1m), has a high selectivity for NE (> 350-fold selectivity for NE
119 over DA) (33). However, current DA biosensors do not have high enough selectivity for DA over NE
120 [Green-DA biosensors: dLight1.1 (60-fold, but see *SI Appendix*, Fig. S7), GRAB_{DA1h} (~ 10-fold), and
121 GRAB_{DA2m} (15-fold); Red-DA biosensor: rGRAB_{DA1m} (22-fold)] (31, 32, 34) and consequently, it is
122 difficult to use these DA biosensors for the simultaneous detection of DA and NE.

123 To image DA and NE dynamics simultaneously with high spatial and temporal resolution, we
124 developed a red-DA biosensor using circular-permutated mApple (cpmApple), which has high selectivity
125 for DA (143-fold selectivity for DA over NE). Using this red-DA biosensor with the existing green-NE
126 biosensor, NE1m, which has high selectivity for NE (33), allowed us to successfully perform dual-color
127 fluorescence monitoring of DA and NE with live imaging in both HeLa cells and primary culture of rat
128 hippocampal neurons *in vitro*.

129 **Results**

130 **Development and characterization of a red-DA biosensor.** To develop a genetically encoded red
131 fluorescence DA biosensor, we adopted the same approach as used to develop the green-DA sensors
132 dLight (31) and GRAB_{DA} (32). First, we constructed an initial red-DA biosensor variant by inserting a
133 red fluorescent protein, cpmApple (35), with linker sequences between Lys 232 and Lys 269 of human
134 DA receptor D1 (DRD1), similarly to that done to construct dLight. We named it red fluorescent
135 genetically encoded GPCR activation reporter for DA, ‘R-GenGAR-DA1.0’ (abbreviated DA1.0; Fig.
136 1A). However, when DA was applied, DA1.0 did not exhibit a fluorescence response (*SI Appendix*, Fig.
137 S1A). To improve its fluorescence response to DA, random mutagenesis was performed on the linker
138 peptide sequences between DRD1 and cpmApple on DA1.0 (Fig. 1A). HeLa cells expressing mutants of
139 DA1.0 were stimulated by application of DA, and the change in red fluorescence intensity was quantified
140 (Fig. 1B). Of 864 mutants, we selected three mutants (#76, #310, and #430) that responded positively to
141 DA and subjected them to time-lapse imaging (Fig. 1 C and D, and *SI Appendix*, Fig. S1B). All three
142 mutants showed detectable red fluorescence increases in response to DA application and this response
143 was blocked by the DRD1/5 antagonist SCH 23390 (SCH) (Fig. 1 C and D, and *SI Appendix*, Fig. S1B).
144 The amino acid sequences of mutated linkers were determined in these mutants (*SI Appendix*, Fig. S1C).
145 We selected #76 (‘R-GenGAR-DA1.1’, abbreviated DA1.1) because it showed the largest positive
146 response to DA amongst the three mutants. We then characterized the dose-response curves of DA1.1
147 for DA and NE and calculated the half maximal effective concentration (EC₅₀). As a result, DA1.1
148 showed 12.6-fold selectivity for DA over NE (Fig. 1E).

149

150 **Development and characterization of an inverse-type red-DA biosensor.** The dynamic range of
151 DA1.1 and its selectivity for DA were lower than some other DA biosensors (31, 32, 34), prompting us
152 to make further improvements. We attempted to expand the dynamic range of DA1.1 by introducing the
153 same mutations as in the green-DA biosensor dLight1 (31). Substitution of Phe 129 with Ala (F129A

154 mutation of dLight1.2; *SI Appendix*, Fig. S2A), and addition of Glu to the N-terminal linker (dLight1.3a;
155 Fig. 2A) were previously shown to significantly increase the dynamic range of dLight1.1 (31). The
156 F129A mutation in DA1.1, however, led to only a slight increase in the fluorescent signal upon DA
157 application (*SI Appendix*, Fig. S2B) and its sensitivity to both DA and NE was lower than that of the
158 original DA1.1 (data not shown). Surprisingly, the addition of Glu to the N-terminal linker in DA1.1
159 showed bright red fluorescence in the basal state. This variant had substantially reduced fluorescence
160 signal in response to DA, which subsequently returned to basal level following treatment with SCH (Fig.
161 2B). We named this inverse type red fluorescence DA biosensor ‘R-GenGAR-DA1.2’ (abbreviated
162 DA1.2).

163 Unexpectedly, time-lapse imaging of DA1.2 in HeLa cells showed that the baseline fluorescent
164 signals increased gradually in both vehicle and control conditions (data not shown). We explored the
165 cause of this phenomenon and found that the DA1.2 baseline fluorescent signals were seemingly
166 associated with thermochromism and photochromism stemming from cpmApple (36) (*SI Appendix*, Fig.
167 S3). The former effect, thermochromism, was apparent from the inverse relationship between baseline
168 fluorescent signals of R-GenGAR-DA and incubation temperature (*SI Appendix*, Fig. S3 A–D).
169 Thermochromism was observed when test compounds were added to our experimental system. Therefore,
170 imaging was performed after temperature equilibration (*SI Appendix*, Fig. S4 and Fig. S5). With respect
171 to photochromism, irradiating light at wavelengths of either 488 nm or 561 nm induced an increase in
172 basal red fluorescence of DA1.2 expressed in HeLa cells under constant medium temperature (*SI*
173 *Appendix*, Fig. S3E). This effect was most pronounced when the irradiation light was at full power.
174 Because light of 488 nm and 561 nm is generally used to excite green and red fluorophores respectively,
175 it was problematic that the photochromism on DA1.2 was induced by the irradiation of those light
176 wavelengths, especially when we combined DA1.2 with another fluorescent biosensor to perform dual-
177 color time-lapse imaging in HeLa cells and primary hippocampal neurons (Fig. 3 and Fig. 5). We found
178 that the increased baseline fluorescence observed in DA1.2 in primary hippocampal neurons was reduced

179 following irradiation of two streams of light (561 nm followed by 488 nm) for 150 s (*SI Appendix*, Fig.
180 S3F). Therefore, pre-light exposure just prior to dual-color time-lapse imaging was conducted to reduce
181 the photochromism effect in DA1.2 (Fig. 3 and Fig. 5, *SI Appendix*, Fig. S5D and Table S1). Time-lapse
182 imaging of DA1.2 with temperature equilibration (*SI Appendix*, Fig. S5B) showed that DA application
183 lowered red fluorescence, which was restored following SCH treatment (Fig. 2C). Baseline fluorescence
184 intensity still increased moderately in both vehicle and control conditions, possibly due to
185 photochromism. The dose-response curve with temperature equilibration (*SI Appendix*, Fig. S4D–F)
186 shows that DA1.2 has a slightly higher dynamic range and comparable affinity to DA ($\max \Delta F/F_0 = -$
187 $0.40 \pm 0.01\%$ and $EC_{50} = 0.68 \pm 0.08 \mu\text{M}$) compared to that of DA1.1 (Fig. 2D). It is of note that the
188 selectivity of DA1.2 for DA over NE was 143-fold, much higher than that of DA1.1 (Fig. 2D), which
189 was due to the decrease in the affinity of DA1.2 to NE. In order to further enhance the selectivity of
190 DA1.2 for DA over NE, we attempted to predict mutations based on ligand-receptor structure models
191 (see *SI Appendix*, Materials and Methods). Since the difference between DA and NE is only one
192 additional hydroxy group on NE, preference for DA might be accomplished by making the area around
193 the binding site unfavorable for this hydroxy group. Based on a structural model complex of the DRD1
194 with either DA or NE in the binding site (*SI Appendix*, Fig. S6A), we then introduced 13 mutations to
195 DA1.2 designed to increase preference for DA over NE (*SI Appendix*, Fig. S6B). Six of the 13 mutants
196 showed a change in red fluorescence response to DA (*SI Appendix*, Fig. S6 C and D). Although the dose-
197 response curves with temperature equilibration for both DA and NE were obtained from three mutants,
198 none of these demonstrated an increase in selectivity for DA over NE compared to that of DA1.2 (*SI*
199 *Appendix*, Fig. S6E). We then confirmed that the selectivity of the red-DA biosensor DA1.2 (143-fold)
200 was higher than that of green-DA biosensors dLight1.1 (17-fold), dLight1.2 (32-fold), and dLight1.3a
201 (19-fold) in our experimental conditions (*SI Appendix*, Fig. S7). Consequently, 143-fold selectivity for
202 DA over NE in DA1.2 is the highest amongst currently available DA biosensors (31, 34).

203 We further characterized how DA1.2 responded to a variety of test compounds. The DRD1/5
204 agonist SKF 81297 led to a partial response from DA1.2, whilst the response to DA was blocked by the
205 DRD1/5 antagonist SCH (Fig. 2E). The application of several other neurotransmitters/neuromodulators
206 showed no significant response in DA1.2 (Fig. 2E). In addition, we confirmed that DA1.2 induced no
207 cyclic adenosine monophosphate (cAMP) increase upon DA application, indicating that, unlike wild-
208 type DRD1, DA1.2 activity does not activate the canonical *Gas* signaling pathway (*SI Appendix*, Fig.
209 S8).

210

211 **Dual-color fluorescence imaging of DA and NE in HeLa cells.** We then tested the simultaneous
212 imaging of DA and NE at the single-cell level. To accomplish this, both DA1.2 and a green-NE sensor,
213 NE1m, which has high selectivity for NE over DA (> 350-fold) (33), were co-expressed in HeLa cells
214 (Fig. 3A). Following irradiation of DA1.2 by two streams of light (561 nm followed by 488 nm) to reduce
215 the effects due to photochromism, we applied the following compounds in this order: NE (1 μ M), DA (5
216 μ M) followed by the α -adrenoceptor antagonist yohimbine (YO, 1 μ M), and SCH (5 μ M) (Fig. 3B and
217 *SI Appendix*, Fig. S5D). As we expected, DA1.2 exhibited a decrease in fluorescence to DA, but not to
218 NE, and its response to DA was blocked by SCH treatment (Fig. 3 B and C and *SI Appendix*, Fig. S9 A
219 and B), confirming that the decrease in fluorescence could indeed be attributed to DA binding to DA1.2.
220 Meanwhile, NE1m showed an increase in green fluorescence upon application of NE, but not DA, and
221 its fluorescence response recovered to its basal level following YO treatment (Fig. 3 B and C and *SI*
222 *Appendix*, Fig. S9 A and B). In summary, we demonstrated that our red-DA biosensor DA1.2 and the
223 existing green-NE biosensor NE1m can distinguish DA and NE, respectively, in HeLa cells.

224

225 **Dual-color fluorescence imaging of DA and NE in a primary culture of rat hippocampal neurons.**
226 To further test the application of DA1.2, we introduced DA1.2 into rat primary hippocampal neurons,
227 where it was successfully expressed, and distributed in plasma membranes throughout neurons (Fig. 4A).

228 Application of DA (5 μ M) led to reduced DA1.2 red fluorescence, and this was restored to baseline by
229 SCH treatment (5 μ M) (Fig. 4 *A* and *B*). Conversely, pretreatment with SCH completely suppressed the
230 response of DA1.2 to DA (Fig. 4*C*), indicating that DA1.2 was successful in facilitating the visualization
231 of DA in primary hippocampal neurons. The dose-response curve for DA with temperature equilibration
232 was obtained in primary hippocampal neurons expressing DA1.2. In this set up, DA1.2 showed max
233 $\Delta F/F_0 = -0.51 \pm 0.05\%$, and an EC_{50} value of $0.56 \pm 0.01 \mu$ M (Fig. 4*D*), which were comparable to the
234 results in HeLa cells.

235 We finally performed dual-color fluorescence imaging of DA and NE in the primary culture of rat
236 hippocampal neurons. DA1.2 and NE1m were co-expressed in the primary hippocampal neurons (Fig.
237 5*A*). After the effects of photochromism were reduced using two streams of light (561 nm followed by
238 488 nm), we then applied compounds in the following order: NE (1 μ M), DA (5 μ M) followed by YO
239 (1 μ M), and SCH (5 μ M) (*SI Appendix*, Fig. S5*D*). As we observed in HeLa cells, DA, but not NE
240 application, led to a decrease in the red fluorescence signal of DA1.2, which was restored following SCH
241 treatment (Fig. 5 *B* and *C* and *SI Appendix*, Fig. S9 *C* and *D*). In addition, we observed a NE-induced
242 increase in NE1m green fluorescence, and this fluorescence response was blocked by YO treatment (Fig.
243 5 *B* and *C* and *SI Appendix*, Fig. S9 *C* and *D*).

244

245

246 **Discussion**

247 We have developed genetically encoded red fluorescent DA sensors R-GenGAR-DA1.1 and DA1.2,
248 which respond positively and negatively to DA, respectively. Specifically, DA1.2 demonstrated
249 reasonable dynamic range ($\Delta F/F_0 = -50\%$) and DA affinity ($EC_{50} = 0.7 \mu$ M) as well as high selectivity
250 for DA (143-fold higher affinity than for NE). In HeLa cells, dual-color live imaging of DA and NE was
251 successfully performed using DA1.2 combined with the existing green-NE biosensor NE1m, which has
252 high selectivity for NE over DA (> 350 -fold) (33). Furthermore, DA1.2 and NE1m were also co-

253 expressed in the primary culture of rat hippocampal neurons, allowing dual-color live imaging of DA
254 and NE *in vitro*. We thus successfully demonstrated that application of two different color-based
255 fluorescent neurochemical sensors (i.e. cpGFP- and cpmApple-based sensors) with high selectivity for
256 each ligand allow us to monitor two different neurochemicals simultaneously.

257 A striking feature of DA1.2 is its high selectivity for DA over NE. For a DA biosensor, selectivity
258 for DA over NE is critical to avoid cross-reactivity for imaging in the brain areas where NE is present at
259 relatively higher amount than DA (5, 28, 37, 38). In our experimental conditions, the specificity for DA
260 over NE, shown by green-DA biosensor dLight1 variants, was lower than that in a previous study (31):
261 dLight1.1 (17-fold), dLight1.2 (32-fold), dLight1.3a (19-fold) (*SI Appendix*, Fig. S7). Sun and colleagues
262 reported that DA biosensors GRAB_{DA} also did not have enough selectivity for DA over NE: GRAB_{DA1h}
263 (~10-fold), GRAB_{DA2m} (15-fold), and rGRAB_{DA1m} (22-fold) (32, 34). Thus, DA1.2 has the highest
264 selectivity for DA over NE (143-fold) compared to all other currently available DA biosensors. Although
265 we tried to further increase the selectivity of DA1.2 by introducing mutations predicted from *in silico*
266 models (*SI Appendix*, Fig. S6), the selectivity of DA1.2 was not raised above the already obtained 143-
267 fold level, possibly due to the use of models in the absence of the crystal structure of DRD1. Taking
268 advantage of this high selectivity of DA1.2 for DA over NE, we succeeded in detecting DA and NE
269 simultaneously in HeLa cells and primary hippocampal neurons *in vitro* by dual-color imaging combined
270 with the existing green-NE biosensor NE1m, which has the highest selectivity for NE over DA (33). The
271 affinity of DA1.2 to DA ($EC_{50} = 0.68 \mu\text{M}$ in HeLa cells, and $EC_{50} = 0.56 \mu\text{M}$ in primary hippocampal
272 neurons) was at sub-micromolar levels, which is within the range of available DA biosensors, comparable
273 to the dLight1 series (31) and lower than the GRAB_{DA} series (32, 34). In addition, other advantages of
274 the red fluorescent DA1.2 sensor are lower phototoxicity and higher tissue penetration because of its
275 longer excitation wavelength. Furthermore, DA1.2 enables multiplex imaging with other colored
276 biosensors for different neurochemicals (39, 40), optogenetic actuators (41), intracellular signaling
277 biosensors (42, 43), calcium indicators (44, 45), and voltage indicators (46).

278 Despite the successful simultaneous imaging of DA and NE using DA1.2 combined with NE1m *in*
279 *vitro*, further improvements to DA1.2 will be required for use in *in vivo* imaging. The main areas in which
280 improvement are required are: [i] expanding the dynamic range and [ii] lowering thermochromism and
281 photochromism. The first concern is the relatively low dynamic range DA1.2 ($\Delta F/F_0 \sim -50\%$). Recent
282 literature on biosensor development has shown that an increase in dynamic range can be achieved by
283 optimization of the linker insertion site, linker length, and, by random mutagenesis, the amino acid
284 sequences on the linkers and the circular-permuted fluorescent protein (34, 47, 48). In order to expand
285 the dynamic range of DA1.2, these strategies should be applied to DA1.2 in future work. The second
286 concern regarding DA1.2 is thermochromism and photochromism, which is due to cpmApple (36). The
287 thermochromic effect could potentially be avoided if the temperature of the animal is kept constant during
288 *in vivo* imaging. In addition, it was recently reported that photochromism due to a cpmApple was
289 successfully diminished by introduction of 22 mutations in the cpmApple region of red-dopamine sensor
290 rGRAB_{DA} (34). Therefore, it may be possible to minimize photochromism in DA1.2 by introducing these
291 mutations into cpmApple. Once those issues are overcome, an improved DA1.2 could be an extremely
292 useful tool for simultaneous measurements of extracellular DA and NE dynamics in the brains of freely
293 moving animals.

294 Recently, there has been an increased demand for the development of tools to observe DA and NE
295 dynamics simultaneously with high spatial and temporal resolution *in vivo*. For example, it was reported
296 that pharmacological blockade of dopamine D₁/D₅ receptors in the hippocampus prevented a memory-
297 boosting effect induced by environmental novelty or by optogenetic activation of noradrenergic LC
298 neurons in mice (4). Later, Kempadoo and colleagues directly detected co-release of DA along with NE
299 after optogenetic stimulation of LC axons in the hippocampus *ex vivo* using high-performance liquid
300 chromatography (5). These discoveries raise many questions regarding the co-release of DA and NE
301 from LC terminals into the hippocampus in freely moving animals. For instance, what are the ranges of
302 spatial diffusion and the precise time courses of concentration change? High spatial and temporal dual-

303 color imaging of DA and NE dynamics in the hippocampus could give us an opportunity to answer these
304 questions. Furthermore, when fiber photometry or two-photon microscopy is applied, the dual-color
305 imaging will enable the measurement of DA and NE at the same spot in the brain. Because of this, the
306 extracellular spatiotemporal dynamics of DA and NE will be comparable to each other under the same
307 conditions.

308 To the best of our knowledge, this is the first time that simultaneous live imaging of extracellular
309 DA and NE has been performed with dual-color fluorescence in both HeLa cells and in a primary culture
310 of rat hippocampal neurons *in vitro*. Here, this was accomplished using our red-DA biosensor DA1.2
311 combined with the existing green-NE biosensor NE1m. This approach will be able to provide new
312 insights into the high spatial and temporal dynamics of neuromodulators DA and NE in brain areas of
313 interests, leading to advances in our understanding of the mechanisms of interplay between DA and NE
314 in organizing key brain functions. A better understanding of these neuromodulatory systems would have
315 the potential to facilitate new ways of treating psychiatric disorders and neurodegenerative diseases.

316

317

318 **Materials and Methods**

319 Animal experiments were approved by the Animal Care Committee of the National Institutes of Natural
320 Sciences in Japan (19A029) and were performed in accordance with its guidelines. Details on animals,
321 and procedures regarding drugs, molecular cloning, saturation polymerase chain reaction (PCR) for the
322 screening of optimal linker sequences, design of DRD1 mutations, cell culture, drug administrations,
323 fluorescence imaging, detection of cAMP signaling using cAMP biosensor, quantification of imaging
324 and data analysis, and statistical analysis are detailed in *SI Appendix*, Materials and Methods.

325

326

327 **ACKNOWLEDGMENTS.** We thank all members of the Aoki and Takeuchi laboratories for
328 helpful discussions and assistance. Sachiko Furukawa and Yuri Miyazaki helped with the primary culture
329 of rat hippocampal neurons. The plasmid DNA of GRAB_{NE1m}, RGECO1, and DRD1-Tango was
330 provided by Yulong Li, Takeharu Nagai, and Bryan Roth, respectively. We also thank Takanari Inoue,
331 Adrian Duszakiewicz, David Bett, Mai Iwasaki, Yulong Li, Steffen Sinning, and Lina Bukowski for
332 scientific discussion.

333 This work was supported by Japan Society for the Promotion of Science (JSPS) KAKENHI Grants
334 (no.19K16050 to Y.G.; no. 19H03331 to Y.F.; no. 18H04873 to M.F.); Lundbeckfonden (R163-2013-
335 16327) and Danmarks Frie Forskningsfond | Natural Sciences (8021-00173B) (to D.E.G.); Core Research
336 for Evolutional Science and Technology | Japan Society for the Promotion of Science (JPMJCR1654),
337 JSPS KAKENHI Grants (no. 16KT0069, 16H01425 “Resonance Bio”, 18H04754 “Resonance Bio”,
338 18H02444, and 19H05798), and ONO Medical Research Foundation (to K.A.); Novo Nordisk Fonden
339 Young Investigator Award 2017 (NNF17OC0026774), Aarhus Institute of Advanced Studies (AIAS)-
340 EU FP7 Cofund programme (754513), Lundbeckfonden (DANDRITE-R248-2016-2518), and the
341 Cooperative Study Program (20-105) of National Institute for Physiological Sciences (to T.T.).

342 **References**

- 343 1. J. F. Poulin *et al.*, Mapping projections of molecularly defined dopamine neuron subtypes using
344 intersectional genetic approaches. *Nat Neurosci* **21**, 1260–1271 (2018).
- 345 2. S. D. Robertson, N. W. Plummer, J. de Marchena, P. Jensen, Developmental origins of central
346 norepinephrine neuron diversity. *Nat Neurosci* **16**, 1016–1023 (2013).
- 347 3. L. A. Schwarz *et al.*, Viral-genetic tracing of the input-output organization of a central noradrenaline
348 circuit. *Nature* **524**, 88–92 (2015).
- 349 4. T. Takeuchi *et al.*, Locus coeruleus and dopaminergic consolidation of everyday memory. *Nature*
350 **537**, 357–362 (2016).
- 351 5. K. A. Kempadoo, E. V. Mosharov, S. J. Choi, D. Sulzer, E. R. Kandel, Dopamine release from the
352 locus coeruleus to the dorsal hippocampus promotes spatial learning and memory. *Proc Natl Acad*
353 *Sci U S A* **113**, 14835–14840 (2016).
- 354 6. B. S. Beas *et al.*, The locus coeruleus drives disinhibition in the midline thalamus via a dopaminergic
355 mechanism. *Nat Neurosci* **21**, 963–973 (2018).
- 356 7. W. Schultz, P. Dayan, P. R. Montague, A neural substrate of prediction and reward. *Science* **275**,
357 1593–1599 (1997).
- 358 8. E. E. Steinberg *et al.*, A causal link between prediction errors, dopamine neurons and learning. *Nat*
359 *Neurosci* **16**, 966–973 (2013).
- 360 9. A. A. Hamid *et al.*, Mesolimbic dopamine signals the value of work. *Nat Neurosci* **19**, 117–126
361 (2016).
- 362 10. A. J. Duzskiewicz, C. G. McNamara, T. Takeuchi, L. Genzel, Novelty and dopaminergic modulation
363 of memory persistence: A tale of two systems. *Trends Neurosci* **42**, 102–114 (2019).
- 364 11. B. Panigrahi *et al.*, Dopamine is required for the neural representation and control of movement
365 vigor. *Cell* **162**, 1418–1430 (2015).
- 366 12. M. W. Howe, D. A. Dombeck, Rapid signalling in distinct dopaminergic axons during locomotion
367 and reward. *Nature* **535**, 505–510 (2016).
- 368 13. B. Xing, Y. C. Li, W. J. Gao, Norepinephrine versus dopamine and their interaction in modulating
369 synaptic function in the prefrontal cortex. *Brain Res* **1641**, 217–233 (2016).
- 370 14. Y. Ranjbar-Slamloo, Z. Fazlali, Dopamine and noradrenaline in the brain; Overlapping or dissociate
371 functions? *Front Mol Neurosci* **12**, 334 (2020).

- 372 15. S. J. Sara, The locus coeruleus and noradrenergic modulation of cognition. *Nat Rev Neurosci* **10**,
373 211–223 (2009).
- 374 16. M. E. Carter *et al.*, Tuning arousal with optogenetic modulation of locus coeruleus neurons. *Nat*
375 *Neurosci* **13**, 1526–1533 (2010).
- 376 17. A. Eban-Rothschild, G. Rothschild, W. J. Giardino, J. R. Jones, L. de Lecea, VTA dopaminergic
377 neurons regulate ethologically relevant sleep-wake behaviors. *Nat Neurosci* **19**, 1356–1366 (2016).
- 378 18. E. Isingrini *et al.*, Resilience to chronic stress is mediated by noradrenergic regulation of dopamine
379 neurons. *Nat Neurosci* **19**, 560–563 (2016).
- 380 19. S. Granon *et al.*, Enhanced and impaired attentional performance after infusion of D1 dopaminergic
381 receptor agents into rat prefrontal cortex. *J Neurosci* **20**, 1208–1215 (2000).
- 382 20. M. D. Lapiz, D. A. Morilak, Noradrenergic modulation of cognitive function in rat medial prefrontal
383 cortex as measured by attentional set shifting capability. *Neuroscience* **137**, 1039–1049 (2006).
- 384 21. M. Wang, S. Vijayraghavan, P. S. Goldman-Rakic, Selective D2 receptor actions on the functional
385 circuitry of working memory. *Science* **303**, 853–856 (2004).
- 386 22. S. Vijayraghavan, M. Wang, S. G. Birnbaum, G. V. Williams, A. F. Arnsten, Inverted-U dopamine
387 D1 receptor actions on prefrontal neurons engaged in working memory. *Nat Neurosci* **10**, 376–384
388 (2007).
- 389 23. M. Wang *et al.*, α 2A-adrenoceptors strengthen working memory networks by inhibiting cAMP-HCN
390 channel signaling in prefrontal cortex. *Cell* **129**, 397–410 (2007).
- 391 24. A. F. Arnsten, S. R. Pliszka, Catecholamine influences on prefrontal cortical function: relevance to
392 treatment of attention deficit/hyperactivity disorder and related disorders. *Pharmacol Biochem*
393 *Behav* **99**, 211–216 (2011).
- 394 25. J. M. Beaulieu, R. R. Gainetdinov, The physiology, signaling, and pharmacology of dopamine
395 receptors. *Pharmacol Rev* **63**, 182–217 (2011).
- 396 26. O. Borodovitsyna, M. Flamini, D. Chandler, Noradrenergic modulation of cognition in health and
397 disease. *Neural Plast* **2017**, 6031478 (2017).
- 398 27. P. Devoto, G. Flore, P. Saba, M. Fa, G. L. Gessa, Stimulation of the locus coeruleus elicits
399 noradrenaline and dopamine release in the medial prefrontal and parietal cortex. *J Neurochem* **92**,
400 368–374 (2005).

- 401 28. J. Van Schoors *et al.*, An improved microbore UHPLC method with electrochemical detection for
402 the simultaneous determination of low monoamine levels in *in vivo* brain microdialysis samples. *J*
403 *Pharm Biomed Anal* **127**, 136–146 (2016).
- 404 29. D. L. Robinson, B. J. Venton, M. L. Heien, R. M. Wightman, Detecting subsecond dopamine release
405 with fast-scan cyclic voltammetry *in vivo*. *Clin Chem* **49**, 1763–1773 (2003).
- 406 30. A. G. Beyene *et al.*, Imaging striatal dopamine release using a nongenetically encoded near infrared
407 fluorescent catecholamine nanosensor. *Sci Adv* **5**, eaaw3108 (2019).
- 408 31. T. Patriarchi *et al.*, Ultrafast neuronal imaging of dopamine dynamics with designed genetically
409 encoded sensors. *Science* **360**, eaat4422 (2018).
- 410 32. F. Sun *et al.*, A genetically encoded fluorescent sensor enables rapid and specific detection of
411 dopamine in flies, fish, and mice. *Cell* **174**, 481–496 e419 (2018).
- 412 33. J. Feng *et al.*, A genetically encoded fluorescent sensor for rapid and specific *in vivo* detection of
413 norepinephrine. *Neuron* **102**, 745–761 e748 (2019).
- 414 34. F. Sun *et al.*, New and improved GRAB fluorescent sensors for monitoring dopaminergic activity *in*
415 *vivo*. *bioRxiv* <https://doi.org/10.1101/2020.03.28.013722> (2020).
- 416 35. Y. Zhao *et al.*, An expanded palette of genetically encoded Ca²⁺ indicators. *Science* **333**, 1888–1891
417 (2011).
- 418 36. Y. Shen, M. D. Wiens, R. E. Campbell, A photochromic and thermochromic fluorescent protein.
419 *RSC Adv.* **4**, 56762–56765 (2014).
- 420 37. J. A. Ihalainen, P. Riekkinen, Jr., M. G. Feenstra, Comparison of dopamine and noradrenaline release
421 in mouse prefrontal cortex, striatum and hippocampus using microdialysis. *Neurosci Lett* **277**, 71–
422 74 (1999).
- 423 38. P. Devoto, G. Flore, On the origin of cortical dopamine: Is it a co-transmitter in noradrenergic
424 neurons? *Current Neuropharmacology* **4**, 115–125 (2006).
- 425 39. A. V. Leopold, D. M. Shcherbakova, V. V. Verkhusha, Fluorescent biosensors for neurotransmission
426 and neuromodulation: engineering and applications. *Front. Cell. Neurosci.* **13**, 474 (2019).
- 427 40. L. Ravotto, L. Duffet, X. Zhou, B. Weber, T. Patriarchi, A bright and colorful future for g-protein
428 coupled receptor sensors. *Front. Cell. Neurosci.* **14**, 67 (2020).
- 429 41. C. K. Kim, A. Adhikari, K. Deisseroth, Integration of optogenetics with complementary
430 methodologies in systems neuroscience. *Nat Rev Neurosci* **18**, 222–235 (2017).

- 431 42. M. Machacek *et al.*, Coordination of Rho GTPase activities during cell protrusion. *Nature* **461**, 99–
432 103 (2009).
- 433 43. S. Mehta *et al.*, Single-fluorophore biosensors for sensitive and multiplexed detection of signalling
434 activities. *Nat Cell Biol* **20**, 1215–1225 (2018).
- 435 44. Y. Okubo *et al.*, Visualization of Ca²⁺ filling mechanisms upon synaptic inputs in the endoplasmic
436 reticulum of cerebellar Purkinje cells. *J Neurosci* **35**, 15837–15846 (2015).
- 437 45. M. Inoue *et al.*, Rational engineering of XCaMPs, a multicolor GECI suite for *in vivo* imaging of
438 complex brain circuit dynamics. *Cell* **177**, 1346–1360 e1324 (2019).
- 439 46. V. Villette *et al.*, Ultrafast two-photon imaging of a high-gain voltage indicator in awake behaving
440 mice. *Cell* **179**, 1590–1608 e1523 (2019).
- 441 47. M. Jing *et al.*, An optimized acetylcholine sensor for monitoring *in vivo* cholinergic activity. *bioRxiv*
442 <https://doi.org/10.1101/861690> (2019).
- 443 48. J. Wan *et al.*, A genetically encoded GRAB sensor for measuring serotonin dynamics *in vivo*. *bioRxiv*
444 <https://doi.org/10.1101/2020.02.24.962282> (2020).

445 **Figure legends**

446 **Fig. 1.** Development of R-GenGAR-DA1.1, which showed a positive response to dopamine (DA). (A)
447 Strategy to develop R-GenGAR-DA1.0. Left panels show a schematic illustration of human DRD1 and
448 the red fluorescent protein ‘cpmApple’ insertion site. Right panels show screening flow chart. Linker
449 sequences connecting DRD1 and cpmApple were randomly mutated using saturation PCR. The plasmids
450 expressing each linker mutant were isolated, followed by the transfection into HeLa cells by lipofection.
451 Changes in fluorescence intensity following 10 μM DA stimulation was monitored by live-cell imaging
452 of HeLa cells expressing each mutant. ICL, intracellular loop; SP, signal peptide (hemagglutinin
453 secretary sequence). (B) Summary of screening results. The normalized fluorescence changes ($\Delta F/F_0$) of
454 the HeLa cells expressing each mutant in response to 10 μM DA stimulation are shown. Each bar
455 represents the average of 1-3 independent experiments. We selected a mutant “R-GenGAR-DA1.1” that
456 showed a maximum response to 10 μM DA stimulation. (C) Representative images of HeLa cells
457 expressing DA1.1 stimulated with 10 μM DA. The fluorescence change ($\Delta F/F_0$) before and after DA
458 stimulation are shown in the pseudocolor intensity-modulated display mode. (D) Normalized
459 fluorescence change ($\Delta F/F_0$) of DA1.1 in HeLa cells in panel C. DA (10 μM) and SCH 23390 (SCH, 10
460 μM) were treated at the time points indicated by pink and blue bars, respectively (*SI Appendix*, Fig. S5A).
461 Mean $\Delta F/F_0$ values of 10 cells from 1 experiment are shown with SD (shaded area). (E) Dose-response
462 curves, with temperature equilibration, of DA (pink) and NE (green) in HeLa cells expressing DA1.1 (*SI*
463 *Appendix*, Fig. S4D). DA: max $\Delta F/F_0 = 0.23 \pm 0.02\%$ and $EC_{50} = 0.45 \pm 0.21 \mu\text{M}$; NE: max $\Delta F/F_0 = 0.17$
464 $\pm 0.03\%$ and $EC_{50} = 5.68 \pm 1.19 \mu\text{M}$ (DA and NE, $n = 3$ experiments in both cases, 10 cells per
465 experiment). Experimental data (dots) were fitted with the Hill equation (lines). DA1.1 has 12.6-fold
466 selectivity for DA over NE.

467

468 **Fig. 2.** Development of R-GenGAR-DA1.2, which showed a negative red fluorescence response to DA.
469 (A) Schematic illustration of a mutation site. Glutamate (Glu) was introduced into the N-terminal side of

470 a linker in DA1.1. (B) Representative images of HeLa cells expressing DA1.2 treated with 10 μ M DA,
471 followed by 10 μ M DRD1/5 antagonist SCH 23390 (SCH). Images are shown in the pseudocolor
472 intensity-modulated display mode. (C) Normalized fluorescence change ($\Delta F/F_0$) of DA1.2 in HeLa cells.
473 Medium temperature was equilibrated before imaging (*SI Appendix*, Fig. S5B). DA (10 μ M) and SCH
474 (10 μ M) were treated at the time points indicated by pink and blue bars, respectively. Mean $\Delta F/F_0$ of 30
475 cells from 3 experiment are shown with SD (shaded area). Vehicle, 10 μ M HCl or water; control, cells
476 were only exposed to emission light. (D) The dose-response curves, with temperature equilibration, of
477 DA (pink) and NE (green) on HeLa cells expressing DA1.2 (*SI Appendix*, Fig. S4D). DA: max $\Delta F/F_0 =$
478 $-0.40 \pm 0.01\%$ and $EC_{50} = 0.68 \pm 0.08 \mu\text{M}$; NE: max $\Delta F/F_0 = -0.45 \pm 0.05\%$ and $EC_{50} = 98 \pm 51 \mu\text{M}$
479 (DA and NE, $n = 4$ experiments in both cases). Experimental data (dots) were fitted with the Hill equation
480 (lines). DA1.2 has 143-fold selectivity for DA over NE. (E) Selectivity of DA1.2 for pharmacological
481 compounds ($n = 3-4$ experiments, 10 cells per experiment; *SI Appendix*, Fig. S5C). All compounds were
482 10 μ M. DRD1 agonist SKF 81297 (SKF), SCH, DRD2 antagonist haloperidol (Halo), epinephrine (Epi),
483 serotonin (5-HT), glutamate (Glu), γ -aminobutyric acid (GABA), histamine (His), and acetylcholine
484 (ACh). For the vehicle condition, there was no significant difference between 10 μ M HCl in H₂O and
485 0.001% dimethyl sulphoxide (DMSO) ($n = 4$ experiments in each, 10 cells per experiment; Mann-
486 Whitney U -test, $P = 0.69$). Therefore, these values were averaged and used as the vehicle condition.
487 Mean $\Delta F/F_0$ values are shown with SEM. One-way ANOVA, $F_{12,38} = 53.11$, $P < 0.0001$; Dunnett's post
488 hoc test (vs vehicle), **** $P < 0.0001$.

489

490 **Fig. 3.** Dual-color fluorescence time-lapse imaging of R-GenGAR-DA1.2 combined with GRAB_{NE1m}
491 in HeLa cells. (A) Representative image of HeLa cells co-expressing DA1.2 and NE1m. (B) Enlarged
492 time-lapse images in the pseudocolor intensity-modulated display mode from the white boxed regions
493 shown in panel A. Bars show the schedule of agonist/antagonist application to both DA1.2 and NE1m.
494 Gray vertical lines indicate time of application. Concentrations: DA and SCH, 5 μ M; NE and YO, 1 μ M.

495 Medium temperature and photochromism were equilibrated before imaging (*SI Appendix*, Fig. S5D). (C)
496 Normalized fluorescence intensity change ($\Delta F/F_0$) of DA1.2 (top) and NE1m (bottom) in HeLa cells co-
497 expressing DA1.2 and NE1m. Vehicle, 10 μM HCl in H_2O or 0.001% DMSO; control, cells were only
498 exposed to emission light. Mean $\Delta F/F_0$ values of 30 cells from 3 experiments are shown with SD (shaded
499 areas). Result of statistical test is shown in *SI Appendix*, Fig. S9 A and B.

500

501 **Fig. 4.** Characterization of R-GenGAR-DA1.2 in the primary culture of rat hippocampal neurons. (A)
502 Representative images of a primary hippocampal neuron expressing DA1.2. The fluorescence change
503 ($\Delta F/F_0$) before (left) and after the application of 5 μM DA (middle) followed by 5 μM SCH (right) (*SI*
504 *Appendix*, Fig. S5B) are shown in pseudocolor intensity-modulated display mode. Bottom: magnification
505 of dendrite marked in the top left image (white rectangle). Medium temperature was equilibrated before
506 imaging. (B) Normalized fluorescence change ($\Delta F/F_0$) of DA1.2 in the primary hippocampal neurons in
507 panel A. DA (5 μM) and SCH (5 μM) were treated at the time points indicated by pink and blue bars,
508 respectively. Mean $\Delta F/F_0$ values of 6 neurons from 6 experiments are shown with SD (shaded area). (C)
509 DA1.2 was pre-treated with SCH before application of DA. Mean $\Delta F/F_0$ of 3 neurons from 3 experiments
510 are shown with SD (shaded area). Medium temperature was equilibrated before imaging. (D) The dose-
511 response curve with temperature equilibration of DA (pink) on the primary hippocampal neurons
512 expressing DA1.2 (*SI Appendix*, Fig. S4D). DA: max $\Delta F/F_0 = -0.51 \pm 0.05\%$ and $\text{EC}_{50} = 0.56 \pm 0.01$
513 μM ; $n = 7$ neurons from 7 experiments. Experimental data (dots) were fitted with the Hill equation (lines).

514

515 **Fig. 5.** R-GenGAR-DA1.2 combined with GRAB_{NE1m} enables dual-color fluorescence imaging of DA
516 and NE in a primary culture of rat hippocampal neurons. (A) Representative image of a primary
517 hippocampal neuron co-expressing DA1.2 and NE1m. (B) Enlarged time-lapse images of DA1.2 and
518 NE1m treated with agonists or antagonists in pseudocolor intensity-modulated display mode from the
519 dendritic region in the primary hippocampal neurons marked as the white boxes in panel A.

520 Concentrations: DA and SCH, 5 μ M; NE and YO, 1 μ M. Medium temperature and photochromism were
521 equilibrated before imaging (*SI Appendix*, Fig. S5D). (C) Normalized fluorescence intensity change
522 ($\Delta F/F_0$) of DA1.2 (top) and NE1m (bottom) in the primary hippocampal neurons co-expressing DA1.2
523 and NE1m. Bars show the schedule of agonist/antagonist application to both DA1.2 and NE1m. Gray
524 vertical lines indicate time of application. Vehicle, 10 μ M HCl in H₂O or 0.001% DMSO; control, cells
525 were only exposed to emission light. Colored lines indicate mean $\Delta F/F_0$ and light-colored shaded area is
526 the SD. Ligands, 6 neurons from 6 experiments; vehicles, 4 neurons from 4 experiments; control, 4
527 neurons from 1 experiment. Statistical test results are shown in *SI Appendix*, Fig. S9 C and D.

1 **Supplementary Information**

2

3 **A genetically encoded red fluorescence dopamine biosensor enables dual imaging of** 4 **dopamine and norepinephrine**

5

6 Chihiro Nakamoto, Yuhei Goto, Yoko Tomizawa, Yuko Fukata, Masaki Fukata, Kasper Harpsøe, David
7 E. Gloriam, Kazuhiro Aoki, and Tomonori Takeuchi

8

9

10 **Materials and Methods**

11 **Animals**

12 Pregnant Wistar/ST rats were purchased from Japan SLC, Inc. for the primary cultures of rat hippocampal
13 neurons. All experiments were approved by the Animal Care Committee of the National Institutes of
14 Natural Sciences in Japan (19A029), and were performed in accordance with its guidelines.

15

16 **Compounds used to test fluorescence response**

17 Dopamine (DA) hydrochloride (1 M stock, H8602, Sigma-Aldrich), serotonin hydrochloride (50 mM
18 stock, 14332, CAY), and L-adrenaline (epinephrine) (5 mM stock, A0173, TCI) were dissolved in 10
19 mM HCl. L-noradrenaline bitartrate monohydrate (1 M stock, A0906, TCI), sodium L-glutamate
20 monohydrate (10 mM stock, G0188, TCI), 4-aminobutyric acid (100 mM stock, A0282, TCI), histamine
21 (100 mM stock, 18111-71, Nacalai Tesque), acetylcholine chloride (10 mM stock, A6625, Sigma-
22 Aldrich), and R(+)-SCH 23390 hydrochloride (10 mM stock, D054, Sigma-Aldrich) were each dissolved
23 separately in distilled water. SKF 81297 hydrobromide (10 mM stock, 1447, TOCRIS), haloperidol

24 hydrochloride (20 mM stock, 0931, TOCRIS), and yohimbine hydrochloride (20 mM stock, 1127,
25 TOCRIS) were dissolved in DMSO. Compound solutions were then subdivided into aliquots and stored
26 at -20°C until use. A working solution of 1 M DA was stored at 4°C for 3 weeks prior to use.

27

28 **Plasmids**

29 R-GenGAR-DA1.0 cDNA and dLight1.1 (Patriarchi *et al.*, 2018) cDNA were synthesized by FASMAC
30 Co. Ltd. into the vector plasmid pUCFa (FASMAC Co. Ltd.). We used a cpmApple module with linker
31 sequences (LSS-LI-cpmApple-NH-DQL) from RGECO1, which was a kind gift from Dr. Takeharu
32 Nagai (Zhao *et al.*, 2011), for insertion into human DRD1. Sequences coding for hemagglutinin (HA)
33 secretion motif and a FLAG epitope were placed at the 5' end of the construct as in dLight1.1 (Patriarchi
34 *et al.*, 2018) (Fig. 1A). *EcoRI* and *NotI* recognition sites were placed at the 5' and 3' end, respectively,
35 for subcloning into the expression vector, pCAGGS (Niwa *et al.*, 1991) with the ligation by Ligation
36 High ver.2 (TOYOBO). Point mutations of R-GenGAR-DA1, and dLight1.2 and dLight1.3a (Patriarchi
37 *et al.*, 2018) were made using polymerase chain reaction (PCR) with the primers containing each
38 mutation and PCR enzyme mixture KOD One (TOYOBO). GRAB_{NE1m} (Feng *et al.*, 2019) was provided
39 by Dr. Yulong Li and subcloned into the pCAGGS.

40

41 **Saturation PCR for the screening of optimal linker sequence**

42 To maximize the chromophore fluorescence changes according to the conformational change of R-
43 GenGAR-DA1.0, optimized linker sequences were screened by the saturated PCR. Primers with random
44 bases encoding two-amino acid length were designed as follows. Forward Primer: 5'-
45 TTGCTCAGAACTTTCAAGTNNBNNBGTGTCCGAAAGAATGTACCC-3'; Reverse Primer: 5'-
46 GTTTCTCTTTTCAACTGATCVNNVNNTGCCTCCCACCCCATAGTTT-3'.

47 Randomized linker sequences and cpmApple were amplified by PCR and inserted into pUCFa-

48 DRD1-cpmApple plasmid with NEBuilder (NEB). This mutant library was transformed into *E.coli* and
49 the plasmid library was prepared from the mixture of transformed *E.coli*. Library plasmids were digested
50 by *EcoRI* and *NotI* to extract library insert. Library inserts were subcloned into the pCAGGS vector by
51 ligation and transformation into *E.coli*. Single *E.coli* colonies were picked up and the plasmids were
52 prepared from them. Each plasmid was transfected into HeLa cells seeded in 96-well glass-bottom plate
53 with 293-fectin (Thermo Fisher Scientific). Two days after the transfection, cells were imaged as
54 described below.

55

56 **Design of DRD1 mutations based on structural models**

57 Structural models of DRD1 with DA and NE were constructed using PyMOL (The PyMOL Molecular
58 Graphics System, Version 2.0 Schrödinger, LLC) from a crystal structure of the related β_2 -adrenoceptor
59 with bound epinephrine (Ring *et al.*, 2013) downloaded from the RCSB Protein Data Bank web site
60 (<http://www.pdb.org>; PDB code, 4LDO). The binding site residues with side-chain atoms within 5 Å of
61 epinephrine's aliphatic hydroxy group was exchanged for those of DRD1 by selecting high-probability
62 backbone-dependent rotamers suggested by the mutagenesis wizard in PyMOL. DA was built by deleting
63 the additional methyl plus aliphatic hydroxy group and NE by deleting only the methyl group. Using the
64 same cut-off as above, Ser 107, Val 317 and Trp 321 were identified as residues that could potentially
65 interact with the extra hydroxy group on NE. Asp 103 was disregarded as it is essential for binding of
66 both agonists by interacting with the protonated amine.

67 With the aim of lowering the binding affinity of NE by removing a potential hydrogen bond to the
68 aliphatic hydroxy of NE, Ser 107 was mutated to Cys and Ala. Additionally, to introduce steric hinderance
69 around the aliphatic hydroxy group, Ile, Leu, Met and Val mutations were also performed. Val 317 was
70 mutated to other hydrophobic residues with longer side chains, that is, Ile, Leu, Phe and Met, again to
71 introduce steric hinderance around the hydroxy in NE. Trp 321 was first mutated to Phe to remove the

72 hydrogen bonding possibility whilst maintaining aromaticity, but since this was detrimental to DA and
73 NE binding, we attempted other residues that maintained hydrogen bonding possibility, that is, His and
74 Gln.

75

76 **Cell culture**

77 HeLa cells were purchased from the Human Science Research Resources Bank. HeLa cells were cultured
78 in DMEM (Wako) supplemented with 10% fetal bovine serum (Sigma-Aldrich) at 37 °C in 5% CO₂.
79 HeLa cells (3×10^4 cells/well) were plated on CELLview cell culture dishes (glass bottom, 35 mm
80 diameter, 4 compartments; The Greiner Bio-One) (*SI Appendix*, Fig. S4A) one day before transfection.
81 Transfection was performed by incubating the cells with a mixture containing 250 ng DNA and 0.25 µl
82 293fectin transfection reagent (Thermo Fisher Scientific) per well for 4-6 h. Imaging was performed 2
83 days after transfection.

84 Primary cultures of rat hippocampal neurons were prepared similarly to that described previously
85 (Fukata *et al.*, 2013). Pregnant Wistar/ST rats were purchased from Japan SLC, Inc. A pregnant rat with
86 embryonic rats (embryonic days 19) was killed by CO₂ inhalation and then embryos (10 embryos per
87 pregnant rat) were removed and decapitated. Hippocampi were dissected from embryonic rat brains and
88 placed in a 10 cm dish on ice with a Hanks'-buffered saline (Ca²⁺/Mg²⁺ free; CMF-HBSS) containing:
89 Hanks' Balanced Salt solution (Sigma-Aldrich), 10 mM glucose, and 10 mM Hepes (pH 7.4). To
90 dissociate hippocampal neurons, hippocampi were treated with 10 units/ml papain (Worthington
91 Biochemical) for 10 min at 37 °C. Dissociated neurons were plated onto poly-L-lysine (Sigma-Aldrich)-
92 coated 35 mm-glass bottom dishes (3×10^5 cells/well) (*SI Appendix*, Fig. S4A) with a plating medium
93 containing: neurobasal medium (ThermoFisher Scientific), 10% FBS, and 10 mM Hepes (pH 7.4).
94 Neurons were incubated at 37 °C and 5% CO₂ for 3 h, and then the medium was replaced by a medium
95 containing: neurobasal medium, B-27 supplement (ThermoFisher Scientific), 2 mM GlutaMax

96 supplement-I (ThermoFisher Scientific), and 10 mM Hepes (pH 7.4). Half of the medium was removed
97 and replaced with fresh medium every 7 days. The cultured neurons were transfected at 14-21 days *in*
98 *vitro* by Lipofectamine 2000 (Thermo Fisher Scientific) and were imaged 4-6 days after transfection.

99

100 **Fluorescence imaging**

101 For the imaging of HeLa cells, the medium was changed to imaging buffer [FluoroBrite D-MEM (FB),
102 Life Technologies] supplemented with 1% GlutaMAX (Life Technologies), and 0.2% fetal bovine serum
103 at least 2 h before imaging. For primary hippocampal neurons, the medium was changed to HBSS [119
104 mM NaCl, 5 mM KCl, 2 mM CaCl₂, 25 mM Hepes (pH 7.4), 2 mM MgCl₂, and 33 mM D-glucose]
105 before imaging started.

106 For the screening of optimal linkers, HeLa cells transfected with library plasmids were imaged
107 with a high content imaging system, IXM-XLS (Molecular Device), equipped with an air objective lens
108 (CFI Plan Fluor 10×, NA = 0.30, WD = 16 mm and CFI Plan Apochromat Lambda 20×, NA = 0.75,
109 WD = 1 mm; Nikon), a Zyla 5.5 sCMOS camera (ANDOR) and a SOLA SE II light source (Lumencor).
110 The excitation and fluorescence filter settings were as follows: excitation filter 562/40 (FF01-562/40-25),
111 dichroic mirror 350-585/601-950 (T) (FF593-Di03-25×36), and emission fluorescence filter 624/40
112 (FF01-624/40-25) purchased from Semrock. Fluorescence changes before and after application of 10 μM
113 DA were imaged by the IXM-XLS (Molecular Device).

114 Confocal fluorescence imaging of cells were imaged with an IX83 inverted microscope (Olympus)
115 equipped with a sCMOS camera (Prime, Photometrics), an air objective lens (UPLSAPO 20×, NA =
116 0.75, WD = 0.6 mm or UPLXAPO 20×, NA = 0.8, WD = 0.6 mm; Olympus), an oil objective lens
117 (UPLSAPO 60×, NA = 1.35, WD = 0.15 mm or UPLXAPO 60×, NA = 1.42, WD = 0.15 mm; Olympus)
118 and a spinning disk confocal unit (CSU-W1, Yokogawa Electric Corporation), illuminated with a laser
119 merge module containing 440 nm, 488 nm, and 561 nm lasers. The excitation laser and fluorescence filter

120 settings were as follows: excitation laser, 440 nm [for cyan fluorescent protein (CFP) and fluorescence
121 resonance energy transfer (FRET) with cyclic adenosine monophosphate (cAMP) biosensor)], 488 nm
122 (for NE1m) and 561 nm (for DA1.2); excitation dichroic mirror, DM445/514/640 (for cAMP biosensor;
123 Yokogawa Electric), DM405/488/561 (for NE1m and DA1.2; Yokogawa Electric); emission filters 465-
124 500 nm (CFP for cAMP biosensor; Yokogawa Electric), 500-550 nm (for NE1m and FRET for cAMP
125 biosensor; Yokogawa Electric), and 580-654 nm (for DA1.2; Yokogawa Electric).

126

127 **Compounds used to test fluorescence response**

128 Stock solutions for the compounds were dissolved in the appropriate vehicle and 0.95 ~ 1 μ l in each 1.5-
129 ml microcentrifuge tube was prepared. Compounds were mixed with 0.5 ml imaging buffer from the well
130 and applied to the same well at each time point during the imaging (*SI Appendix*, Fig. S4B). For
131 temperature equilibration of the imaging buffer, 0.5 ml of the imaging buffer was transferred from the
132 well into an empty 1.5-ml microcentrifuge tube and then applied to the buffer in the same well; the
133 procedure repeated 5 times (*SI Appendix*, Fig. S4C). The procedure for the compound application in the
134 time-lapse imaging is shown in *SI Appendix*, Fig. S5. The ‘ligand’ dissolved in the appropriate vehicle
135 was applied at the imaging time point shown by the arrow; the ‘vehicle’ was applied at the same time
136 point. The ‘control’ only had light exposure for evaluating the effects of photochromism.

137

138 **Detection of cAMP signaling using cAMP biosensor**

139 The cAMP biosensor ‘CFP-Epac-YFP (yellow fluorescent protein)’, which was developed based on
140 previous work (Ponsioen *et al.*, 2004), contains monomeric teal fluorescent protein (mTFP), the human
141 RAPGEF3 (EPAC) gene (corresponding to 149-881 a.a.) obtained from HeLa cells with RT-PCR, and
142 mVenus. The cDNA of cAMP biosensor was inserted into pCX4neo vector (Akagi *et al.*, 2003). The
143 plasmid was co-transfected with either DRD1-Tango, which was a gift from Dr. Bryan Roth (Addgene

144 kit # 1000000068) (Kroeze *et al.*, 2015), DA1.2, or empty vector. The cells were imaged 2 days after
145 transfection. The level of cAMP was calculated by the ratio of CFP to FRET, followed with normalization
146 by the baseline value before DA application.

147

148 **Quantification of imaging and data analysis**

149 We used Fiji, a distribution of ImageJ (Schindelin *et al.*, 2012), for the preparation of quantification and
150 measurement of all imaging files. Principally, for all images, background was subtracted and images
151 were registered by StackReg, a Fiji plugin to correct misregistration, if required. Note that the median
152 filter was used for the time-lapse images of the neuron before registration to remove camera noise
153 preventing registration. Then, regions of interests (ROIs) were selected for the first time point in time-
154 lapse imaging or in the images before the compound application, to surround the whole cell body for
155 HeLa cells and a dendrite near the cell body for hippocampal neurons. Mean pixel intensity in ROIs were
156 measured and these data were further analyzed by Python3 (<https://www.python.org>). In order to
157 normalize the fluorescence changes with the amount of biosensor expression, $\Delta F/F_0$ was calculated with
158 the intensity before the compound application as F_0 . The fluorescence change ($\Delta F/F_0$) image is
159 represented as the pseudocolor intensity-modulated display mode, where color represents the relative
160 ratio value, whilst the brightness of the color represents the fluorescence intensity of the source images.

161 To obtain the EC_{50} and the max $\Delta F/F_0$, dose-response curves were fitted with Hill function by
162 Python package Scipy1.4 (SciPy.org). Note that the Hill coefficient was fixed as 1 because no cooperative
163 binding was expected.

164

165 **Statistical analysis**

166 All data were presented as mean, with error bars indicating \pm SEM if not otherwise specified. Statistical
167 analyses were performed using GraphPad Prism8 (GraphPad Software) and Python 3.0 (Python Software

168 Foundation) with SciPy (SciPy.org) and scikit-posthocs (<https://scikit-posthocs.readthedocs.io/>)
169 packages. Data were analyzed using Mann-Whitney *U*-test; Student's *t*-test; one-way ANOVA followed
170 by Dunnett's or Tukey-Kramer's post hoc tests as appropriate to correct for multiple comparisons;
171 Friedman test followed by Conover-Iman test with the Bonferroni-Holm correction to correct for multiple
172 comparisons. In Fig. S3 *E* and *F*, normality assumption was judged from Shapiro-Wilk test and Q-Q plot
173 and variances among conditions was supposed to be equal by Bartlett test. All statistical tests were two-
174 tailed. The level of significance was set $P < 0.05$.

175 **Supplementary Figure legends**

176

177 **Fig. S1.** Screening of R-GenGAR-DA1.1. (A) Time-lapse imaging of R-GenGAR-DA1.0. Mean $\Delta F/F_0$
178 of 10 cells is shown with SD (shaded area). Dopamine (DA, 10 μM) was applied at the time point shown
179 by the pink bar. (B) Time-lapse imaging of DA1.0_310 and DA1.0_430. Mean $\Delta F/F_0$ of 10 cells are
180 shown with SD (shaded area). DA (10 μM) and SCH 23390 (SCH, 10 μM) were treated at the indicated
181 time points shown by pink and blue bars, respectively. (C) The amino acid sequence of linker sequences
182 for DA1.0, DA1.1 (DA1.0_76), DA1.0_310, and DA1.0_430, which were obtained from 1st screening.

183

184 **Fig. S2.** Characterization of R-GenGAR-DA1.1_F129A. (A) Schematic illustration of DA1.1_F129A.
185 Phe 129, located in DRD1 intracellular loop 2, mutated to alanin (F129A). (B) Time-lapse imaging of
186 DA1.1_F129A. DA (10 μM) and SCH (10 μM) were treated at the indicated time points. Mean $\Delta F/F_0$ of
187 20 cells from 2 independent experiments are shown with SD (shaded area).

188

189 **Fig. S3.** Thermochromism and photochromism for R-GenGAR-DA. (A–D) Representative images of
190 HeLa cells expressing DA1.1 (A), and DA1.2 (C) shown in the pseudocolor intensity-modulated display
191 mode in various incubation temperatures. Regression curve of normalized fluorescence intensity change
192 ($\Delta F/F_0$) of DA1.1 (B), and DA1.2 (D) and incubation temperature. Negative correlation between
193 fluorescent intensity and temperature in DA1.1 ($r = -0.960$, 20 cells in 2 experiments) and DA1.2 ($r =$
194 -0.927 , 30 cells in 3 experiments) were observed by Pearson product moment correlation coefficient. (E)
195 Photochromism-induced change in fluorescence intensity of HeLa cells expressing DA1.2 under the
196 indicated conditions (excitation light wavelength, excitation light power, and exposure time). Incubation
197 temperature was constant during time-lapse imaging. Images were taken every 3 s. The colored-lines
198 represent the average values with the SD of them (shaded area) ($n = 10$ cells in each case). Differences

199 amongst area under the curves (AUCs) from 4 exposure conditions were tested as follows. Normality
200 assumption was judged from Shapiro-Wilk test and Q-Q plot. Variances among conditions was assumed
201 equal following Bartlett test ($P = 0.696$). One-way ANOVA was performed ($F_{3,36} = 110$, $P < 0.01$). As a
202 post-hoc analysis, Tukey-Kramer was used for multiple comparisons ($*P < 0.05$, $**P < 0.01$). (F)
203 Repeated time-lapse imaging of DA1.2 in primary hippocampal neuron without application of any
204 compounds. Light irradiation protocol as follows: 1-s exposure of 561 nm followed by 1-s exposure of
205 488 nm; every 3 s for a duration of 150 s. Mean $\Delta F/F_0$ values of first (blue) and second (orange) 150-s
206 imaging are shown the SD of them (shaded area) ($n = 4$ neurons). Although the mean $\Delta F/F_0$ values in
207 first 150-s imaging increased gradually because of the photochromism, those in second 150-s imaging
208 were relatively constant and stable. Difference between AUC of first and second imaging was tested by
209 a two-tailed paired t -test ($P = 0.007$).

210

211 **Fig. S4.** Optimized experimental procedure for the dose-response curve. (A) Dishes for imaging of HeLa
212 cells and primary hippocampal neurons. (B) Application of compounds for imaging. The compounds,
213 mixed with the 0.5 ml imaging buffer from the well of interest, was applied at the time of imaging. (C)
214 Temperature equilibration for imaging. Imaging buffer (0.5 ml out of 1 ml for HeLa cells, and 2 ml for
215 the neurons) from the well of interest transferred to the empty 1.5-ml microcentrifuge tube and returned
216 to the same well; repeated five times. This procedure gradually equilibrated the temperature of the
217 imaging buffer to room temperature and effected the basal fluorescence level of DA1.1 and DA1.2 stable.
218 (D) Procedure for making the dose-response curve. Top: the time course of ligand application and
219 imaging shown by the arrow after temperature equilibration. Application of the diluted ligand, imaged
220 sequentially. Bottom: representative images of DA1.2, negatively responding to DA in a dose-dependent
221 manner. (E) Quantification of snapshots in the HeLa cells expressing DA1.2 in the dose-response curve
222 for DA without (left) or with (right) temperature equilibration. Temperature equilibration effected to

223 stabilize the basal level $\Delta F/F_0$ values of DA1.2. (Left, $n = 4$ cells; right, $n = 3$ cells). (F) Confirmation of
224 basal stability of R-GenGAR-DA1.1, and DA1.2. HeLa cells expressing DA1.1 (left) or DA1.2 (right)
225 were treated with 7 trials of vehicle stimulation after temperature equilibration, showing no change in
226 the mean $\Delta F/F_0$ values with the SEM of them ($n = 3$ experiments in each). The procedure is the same as
227 *SI Appendix*, Fig. S4D.

228

229 **Fig. S5.** Time course of application of compounds for imaging in HeLa cells and primary hippocampal
230 neurons. (A) Compound application for time-lapse imaging without temperature equilibration.
231 Compound or vehicle applied with imaging buffer from the well of interest shown by the arrow. Cells
232 were imaged with the appropriate time exposure (*SI Appendix*, Table S1) acquired every 3 s for a duration
233 of 90 s. (B) Compound application with temperature equilibration for time-lapse imaging. Before
234 compound application, temperature equilibration conducted as shown in *SI Appendix*, Fig. S4C. Cells
235 were imaged with the appropriate time exposure (*SI Appendix*, Table S1) acquired every 3 s for a duration
236 of 90 s. (C) Compound application for checking pharmacological selectivity of DA1.2. Cells were
237 imaged with the appropriate time exposure (*SI Appendix*, Table S1) acquired every 3 s for a duration of
238 60 s. Averaged $\Delta F/F_0$ during 30-60 s of each compound was shown in Fig. 2E. (D) Compound application
239 for dual-color imaging. After temperature equilibration, we conducted dual-color light irradiation (1-s
240 exposure of 561 nm followed by 1-s exposure of 488 nm light irradiation) every 3 s for a duration of 150
241 s, which reduced the effect of photochromism, before the start of the imaging. Cells were dual-color
242 imaged (561 nm followed by 488 nm light irradiation) with the appropriate time exposure (*SI Appendix*,
243 Table S1) acquired every 3 s for a duration of 150 s.

244

245 **Fig. S6.** Introducing structural mutations into R-GenGAR-DA1.2. (A) Prediction of the residues
246 responsible for the selectivity between DA and NE from structural models of the DRD1 (light blue

247 cartoon and white sticks) with either DA (left, salmon sticks) or NE (right, green sticks) in the binding
248 site. The amino acids close to the additional hydroxy of NE (i.e. Ser 107, Val 317 and Trp 321) may be
249 utilized to affect the preference for binding of DA over NE, e.g. by mutation of hydrogen bonding (yellow
250 dotted lines) amino acids with hydrophobic ones. (B) Candidates of structural mutation. (C) Mean $\Delta F/F_0$
251 (20 cells from 2 experiments in each case) are shown with the SD of them (shaded area). DA (10 μM)
252 and SCH (10 μM) were treated at the indicated time points shown by pink and blue bars, respectively.
253 (D) Averaged $\Delta F/F_0$ during DA application (30-s duration) of each mutant was shown as mean \pm SEM.
254 (E) The dose-response curves with temperature equilibration of DA (pink) and NE (green) in HeLa cells
255 expressing DA1.2_V317I, DA1.2_V317M, and DA1.2_W321H (*SI Appendix*, Fig. S4D). DA1.2_V317I:
256 DA: max $\Delta F/F_0 = 0.49 \pm 0.01\%$ and $EC_{50} = 1.10 \pm 0.24 \mu\text{M}$; NE: max $\Delta F/F_0 = 0.47 \pm 0.03\%$ and EC_{50}
257 $= 55 \pm 14 \mu\text{M}$; 50-fold selectivity for DA over NE (DA and NE, $n = 3$ experiments in both cases).
258 DA1.2_V317M: DA: max $\Delta F/F_0 = 0.43 \pm 0.02\%$ and $EC_{50} = 0.66 \pm 0.11 \mu\text{M}$; NE: max $\Delta F/F_0 = 0.42 \pm$
259 0.02% and $EC_{50} = 19.0 \pm 4.1 \mu\text{M}$; 28.8-fold selectivity for DA over NE (DA and NE, $n = 3$ experiments
260 in both cases). DA1.2_W321H: DA: max $\Delta F/F_0 = 0.55 \pm 0.06\%$ and $EC_{50} = 12.0 \pm 7.4 \mu\text{M}$; NE: max
261 $\Delta F/F_0 = 0.62 \pm 0.07\%$ and $EC_{50} = 111 \pm 12 \mu\text{M}$; 9.3-fold selectivity for DA over NE (DA and NE, $n = 3$
262 experiments in both cases). Experimental data (dots) were fitted with the Hill equation (lines).

263

264 **Fig. S7.** Comparison of selectivity for DA over NE between R-GenGAR-DA and dLight1 sensors. (A)
265 Dose-response curve for DA (pink) and NE (green) in HeLa cells expressing dLight1.1, dLight1.2 and
266 dLight1.3a. dLight1.1: DA: max $\Delta F/F_0 = 0.95 \pm 0.054\%$ and $EC_{50} = 0.71 \pm 0.083 \mu\text{M}$; NE: max $\Delta F/F_0 =$
267 $0.78 \pm 0.11\%$ and $EC_{50} = 12 \pm 0.55 \mu\text{M}$ (DA and NE, $n = 4$ independent experiments in both cases).
268 dLight1.2: DA: max $\Delta F/F_0 = 4.2 \pm 0.19\%$ and $EC_{50} = 2.3 \pm 0.32 \mu\text{M}$; NE: max $\Delta F/F_0 = 2.8 \pm 0.25\%$ and
269 $EC_{50} = 73 \pm 5.4 \mu\text{M}$ (DA and NE, $n = 4$ independent experiments in both cases). dLight1.3a: DA: max
270 $\Delta F/F_0 = 4.9 \pm 0.50\%$ and $EC_{50} = 3.8 \pm 0.31 \mu\text{M}$; NE: max $\Delta F/F_0 = 3.9 \pm 0.42\%$ and $EC_{50} = 74 \pm 4.7 \mu\text{M}$

271 (DA and NE, $n = 4$ independent experiments in both cases). (B) Summarized affinity for DA and NE, and
272 selectivity for DA over NE of R-GenGAR-DA1.1, R-GenGAR-DA1.2, dLight1.1, dLigh1.2, and
273 dLight1.3a. Selectivity was calculated using EC_{50} of NE relative to EC_{50} of DA.

274

275 **Fig. S8.** cAMP signaling in HeLa cells expressing R-GenGAR-DA1.2. (A) Schematic illustration of the
276 cAMP biosensor, CFP-Epac-YFP. (B) Representative images of DRD1 (left), DA1.2 (middle), and
277 control (right, empty vector), which were co-expressing CFP-Epac-YFP, before (top) and after (bottom)
278 application of DA shown in the pseudocolor intensity-modulated display mode. (C) Time-lapse imaging
279 of cAMP level (CFP/FRET) in HeLa cells expressing DRD1 (blue), DA1.2 (pink), and control (gray).
280 DA (1 μ M) was treated at the time points shown by the pink bar. Cells were imaged with the appropriate
281 time exposure (*SI Appendix*, Table S1) acquired every 1 min for a duration of 30 min. Mean CFP/FRET
282 of 20 cells in 2 experiments is shown with the SD of them (shaded area).

283

284 **Fig. S9.** Statistical analysis of dual-color imaging of DA1.2 and NE1m in HeLa cells and primary
285 hippocampal neurons. (A and C) Quantification of mean values of time-lapse imaging from Fig. 3 (A)
286 and Fig. 5 (C). Each $\Delta F/F_0$ value for a given compound was normalized by the subtraction of averaged
287 vehicle values along the time course. Bars represent mean \pm SEM $\Delta F/F_0$ values for each consecutive step
288 in the experiment. Each bar represents the mean of the final 15 s (5 time points) of each 30 s condition,
289 which occurs immediately prior to the application of each successive compound. The order of bars from
290 left to right reflects the time course. (HeLa cells $n = 30$ cells, neuron $n = 6$ cells). (B and D) Statistical
291 results of *SI Appendix* Fig.S 9A (B) and 9C (D). There were significant differences between compounds
292 analyzed by Friedman test in HeLa cells (DA1.2, $P < 0.001$; NE1m, $P < 0.001$) and in hippocampal
293 primary neurons (DA1.2, $P < 0.001$; NE1m, $P < 0.001$). Conover-Iman test with the Bonferroni-Holm
294 correction for multiple testing, as a post-hoc analysis, P values are shown in the table. n.s., not significant.

295

296

297

Table S1 Conditions for fluorescent imaging

Figure	Sensor	Cell-type	Microscopy	Filters	Exposure time: laser power
Fig. 1B	DA1.0	HeLa	IXM-XLS 10× (NA = 0.30) 20× (NA = 0.75)	Ex: 562/40 Dichroic: 350-585/601-950 (T) Em: 624/40	1000 ms (Lumen cor 100/255)
Fig. 1D Fig. S1 A & B Fig. S2B	DA1.0 DA1.1	HeLa	IX83 20× (NA = 0.75) 20× (NA = 0.80)	Ex: 561 nm Dichroic: DM405/488/561 Em: 580–654 nm	500 ms (Lumen cor 100/255)
Fig. 1E Fig. 2B–E Fig. S3A–D Fig. S4D Fig. S6C–E	DA1.1 DA1.2	HeLa	IX83 with CSU-W1 20× (NA = 0.75) 20× (NA = 0.80)	Ex: 561 nm Dichroic: DM405/488/561 Em: 580–654 nm	200 ms (ND 100 %)
Fig. S3E	DA1.2	HeLa	IX83 with CSU-W1 20× (NA = 0.75) 20× (NA = 0.80)	Ex1: 561 nm Ex2: 488 nm Dichroic: DM405/488/561 Em1: 580–654 nm Em2: 500-550 nm	Ex1: 1000 ms (ND 100%) Ex1: 1000 ms (ND 50%) Ex1, Ex2: 1000 ms (ND 100%) Ex1, Ex2: 200 ms (ND 50%)
Fig.3	DA1.2 NE1m	HeLa	IX83 with CSU-W1 20× (NA = 0.75) 20× (NA = 0.80)	Ex1: 561 nm Ex2: 488 nm Dichroic: DM405/488/561 Em1: 580–654 nm Em2: 500-550 nm	Ex1: 200 ms (ND 100%) Ex2: 200 ms (ND 100%)
Fig. 4	DA1.2	Neuron	IX83 with CSU-W1 60× Oil (NA = 1.35) 60× Oil (NA = 1.42)	Ex: 561 nm Dichroic: DM405/488/561 Em: 580–654 nm	1000 ms (ND 10 %)
Fig. 5 Fig. S3F	DA1.2 NE1m	Neuron	IX83 with CSU-W1 60× Oil (NA = 1.35)	Ex1: 561 nm Ex2: 488 nm	Ex1: 1000 ms (ND 10 %) Ex2: 1000 ms (ND 5%)

			60× Oil (NA = 1.42)	Dichroic: DM405/488/561 Em1: 580–654 nm Em2: 500-550 nm	
Fig. S7	dLigh1.1 dLight1.2 dLight1.3a	HeLa	IX83 20× (NA = 0.75)	Ex: 488 nm Dichroic: DM405/488/561 Em: DM405/488/561	500 msec (Lumen cor 20/255)
Fig. S8	CFP-Epac -YFP	HeLa	IX83 with CSU-W1 20× (NA = 0.75)	Ex: 440 nm Dichroic: DM445/514/640 Em (CFP): 465-500 nm Em (FRET): 500-550 nm	500 ms (ND 25%) for CFP 500 ms (ND 25%) for FRET

298

299 **References**

- 300 Akagi, T., Sasai, K., and Hanafusa, H. (2003). Refractory nature of normal human diploid fibroblasts
301 with respect to oncogene-mediated transformation. *Proc Natl Acad Sci U S A* *100*, 13567–13572.
- 302 Feng, J., Zhang, C., Lischinsky, J.E., Jing, M., Zhou, J., Wang, H., Zhang, Y., Dong, A., Wu, Z., Wu, H.,
303 *et al.* (2019). A genetically encoded fluorescent sensor for rapid and specific in vivo detection of
304 norepinephrine. *Neuron* *102*, 745–761 e748.
- 305 Fukata, Y., Dimitrov, A., Boncompain, G., Vielemeyer, O., Perez, F., and Fukata, M. (2013). Local
306 palmitoylation cycles define activity-regulated postsynaptic subdomains. *J Cell Biol* *202*, 145–161.
- 307 Kroeze, W.K., Sassano, M.F., Huang, X.P., Lansu, K., McCorvy, J.D., Giguere, P.M., Sciaky, N., and
308 Roth, B.L. (2015). PRESTO-Tango as an open-source resource for interrogation of the druggable human
309 GPCRome. *Nat Struct Mol Biol* *22*, 362–369.
- 310 Niwa, H., Yamamura, K., and Miyazaki, J. (1991). Efficient selection for high-expression transfectants
311 with a novel eukaryotic vector. *Gene* *108*, 193–199.
- 312 Patriarchi, T., Cho, J.R., Merten, K., Howe, M.W., Marley, A., Xiong, W.H., Folk, R.W., Broussard, G.J.,
313 Liang, R., Jang, M.J., *et al.* (2018). Ultrafast neuronal imaging of dopamine dynamics with designed
314 genetically encoded sensors. *Science* *360*, eaat4422.
- 315 Ponsioen, B., Zhao, J., Riedl, J., Zwartkuis, F., van der Krogt, G., Zacco, M., Moolenaar, W.H., Bos,
316 J.L., and Jalink, K. (2004). Detecting cAMP-induced Epac activation by fluorescence resonance energy
317 transfer: Epac as a novel cAMP indicator. *EMBO Rep* *5*, 1176–1180.
- 318 Ring, A.M., Manglik, A., Kruse, A.C., Enos, M.D., Weis, W.I., Garcia, K.C., and Kobilka, B.K. (2013).
319 Adrenaline-activated structure of β_2 -adrenoceptor stabilized by an engineered nanobody. *Nature* *502*,
320 575–579.

321 Schindelin, J., Arganda-Carreras, I., Frise, E., Kaynig, V., Longair, M., Pietzsch, T., Preibisch, S., Rueden,
322 C., Saalfeld, S., Schmid, B., *et al.* (2012). Fiji: an open-source platform for biological-image analysis.
323 Nat Methods 9, 676–682.

324 Zhao, Y., Araki, S., Wu, J., Teramoto, T., Chang, Y.F., Nakano, M., Abdelfattah, A.S., Fujiwara, M.,
325 Ishihara, T., Nagai, T., *et al.* (2011). An expanded palette of genetically encoded Ca²⁺ indicators. Science
326 333, 1888–1891.

327

Figure 1

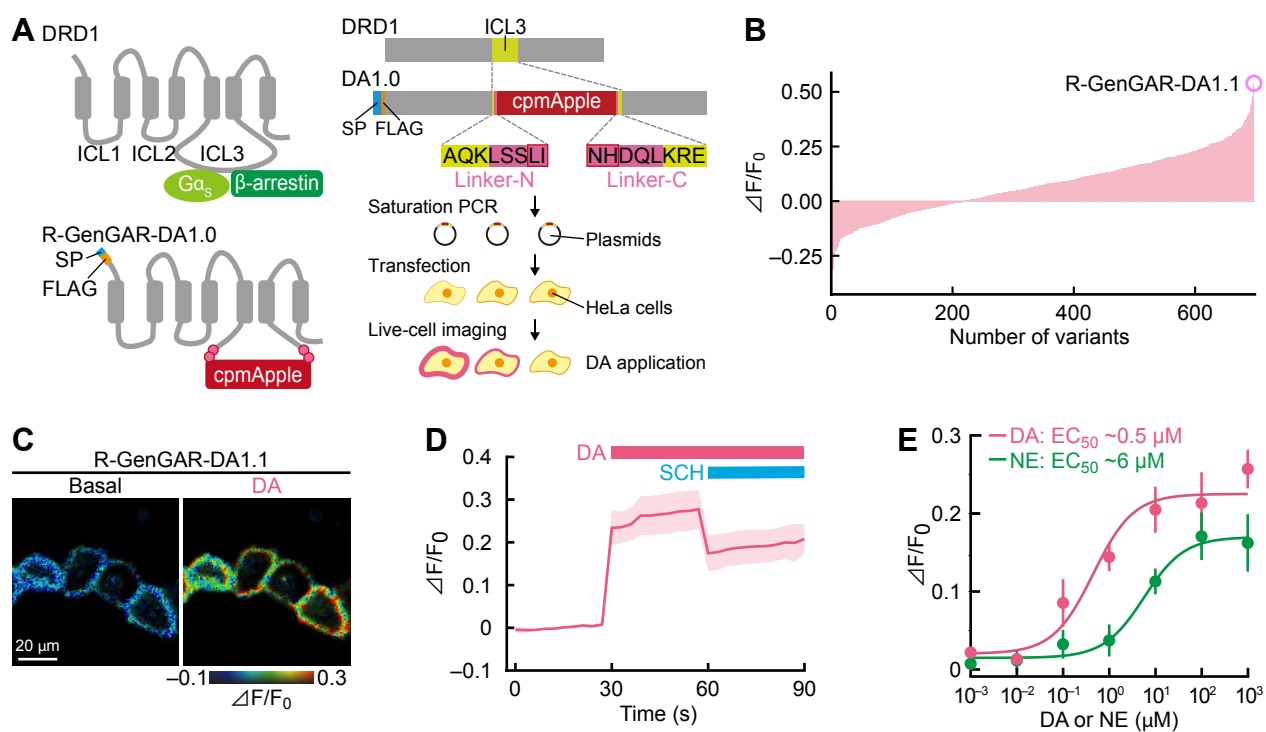


Figure 2

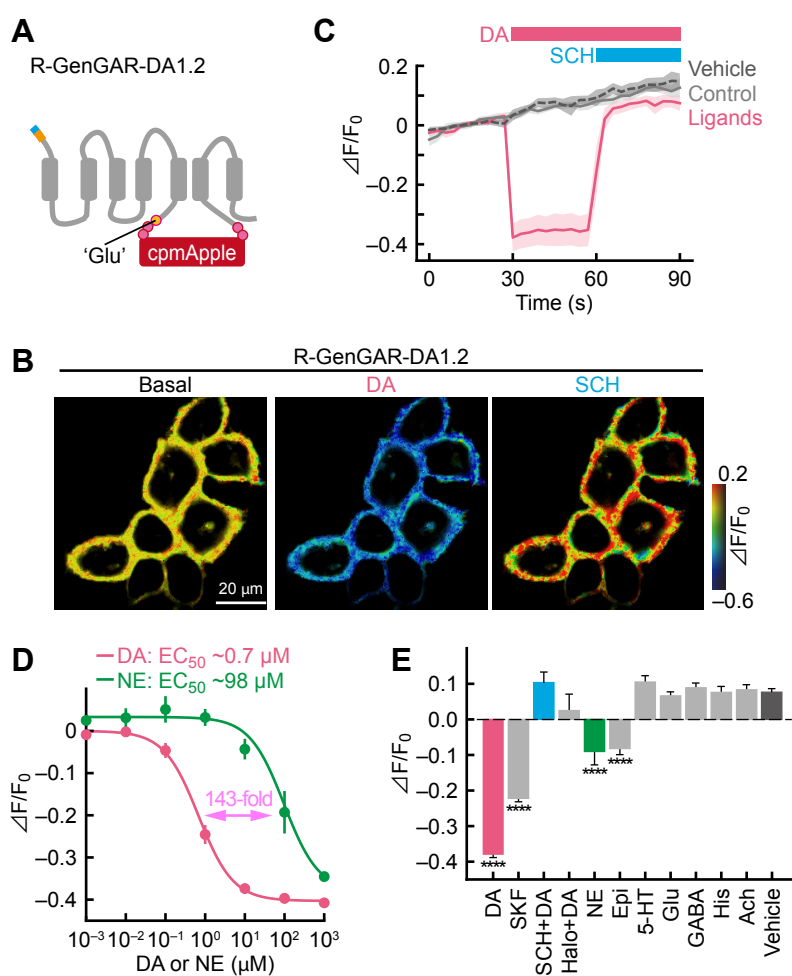


Figure 3

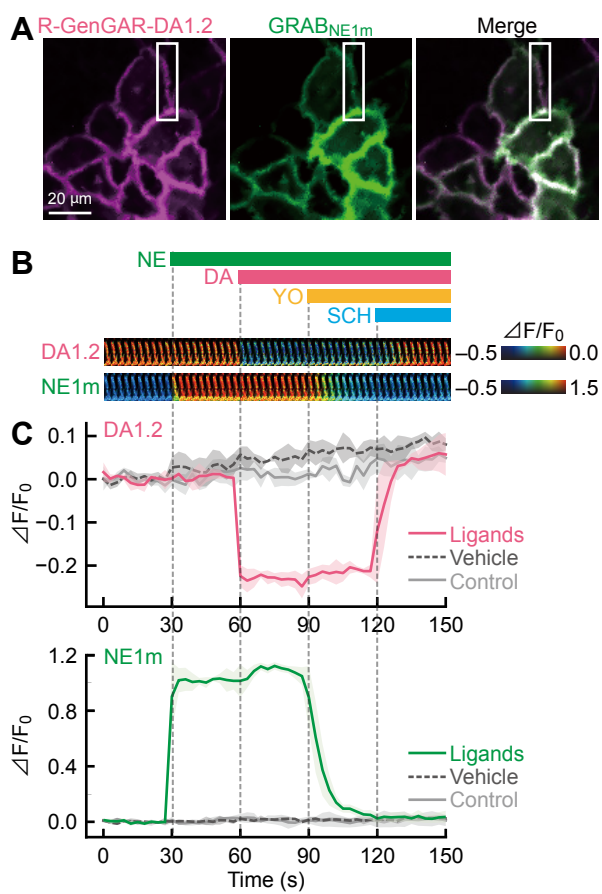


Figure 4

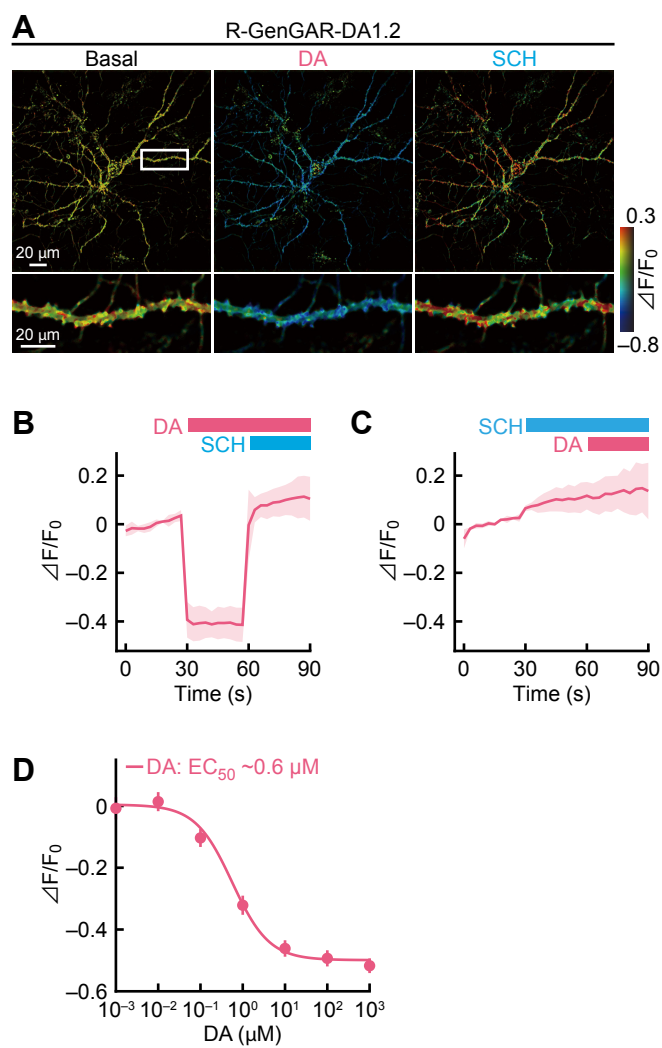


Figure 5

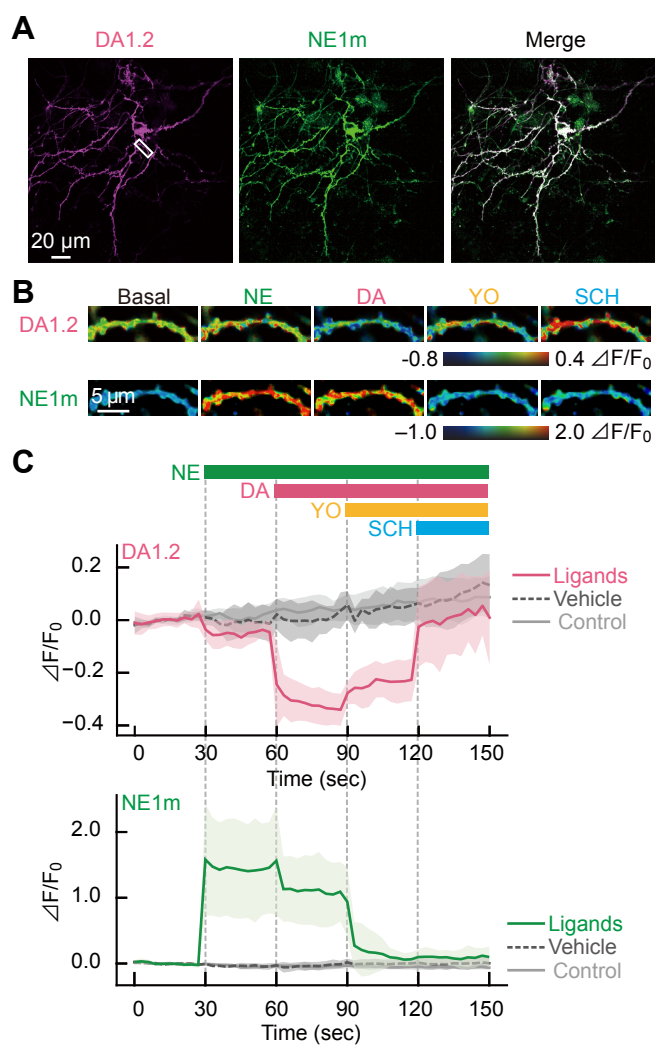


Figure S1

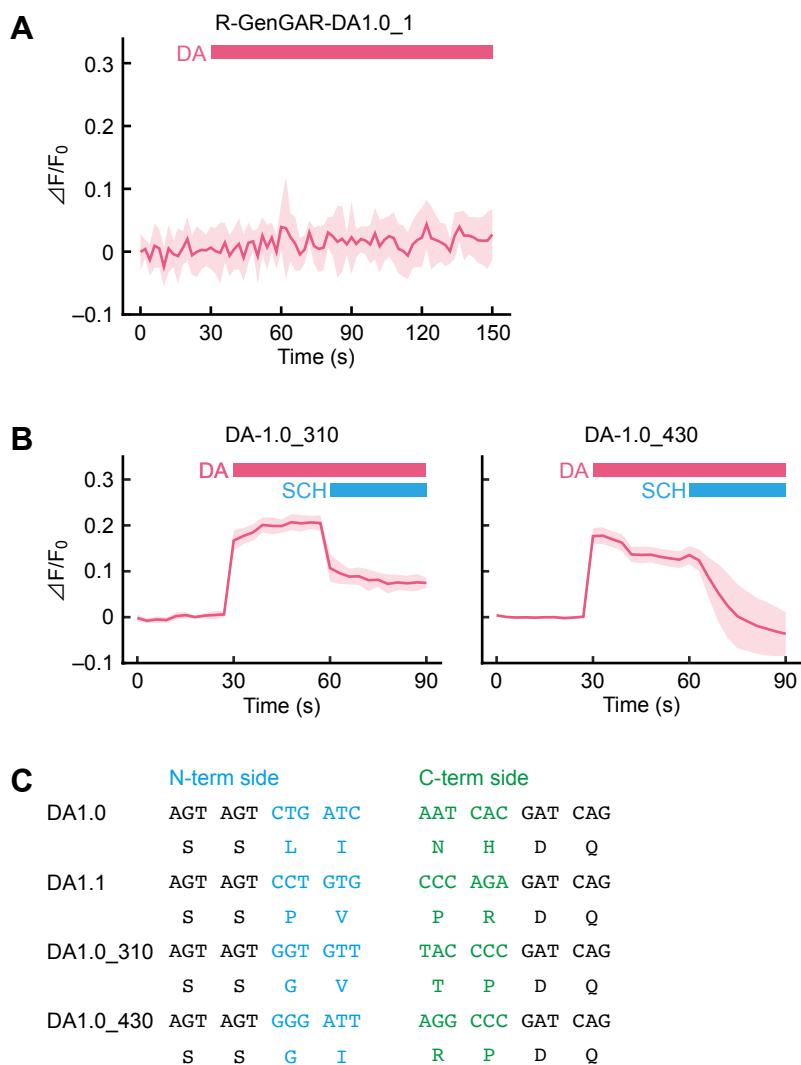


Figure S2

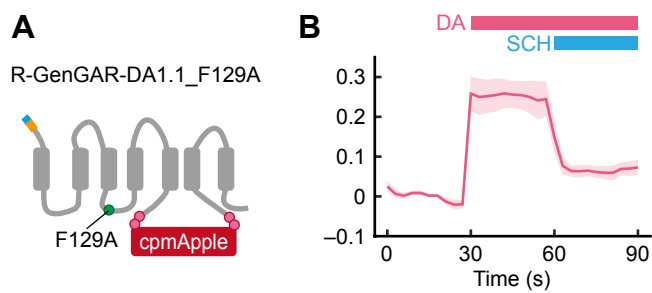


Figure S3

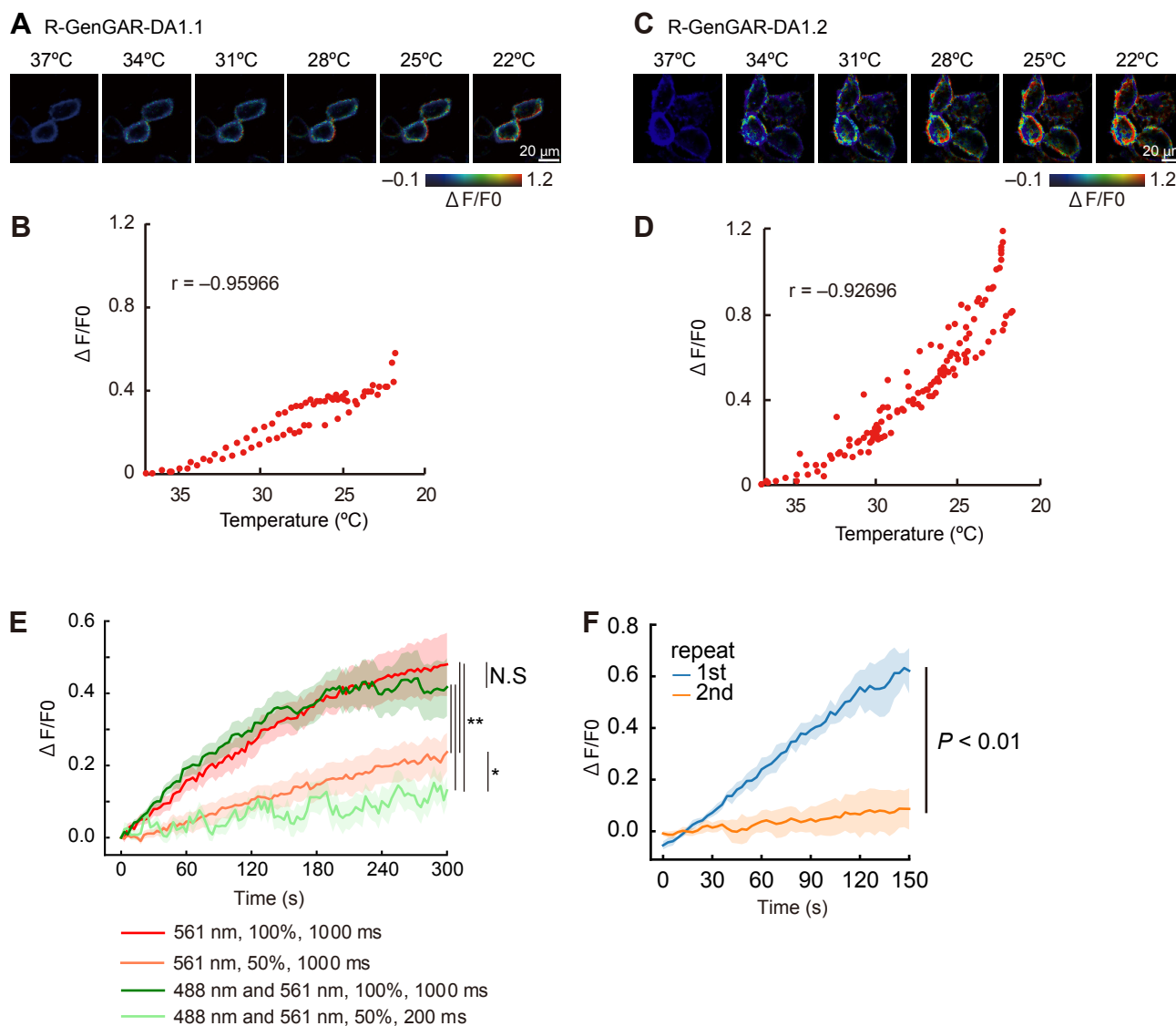
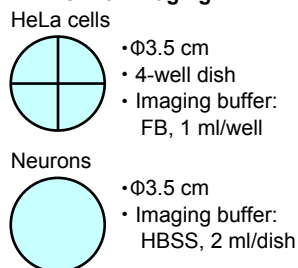
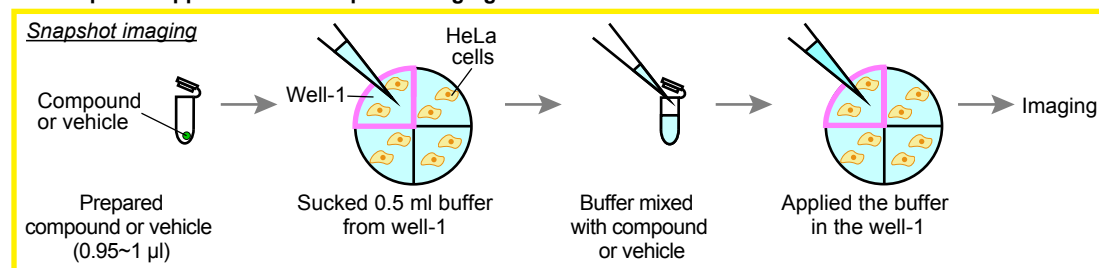


Figure S4

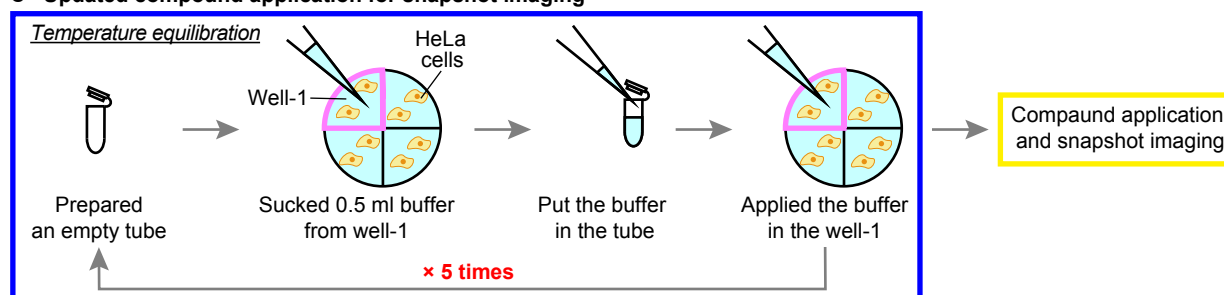
A Dish for Imaging



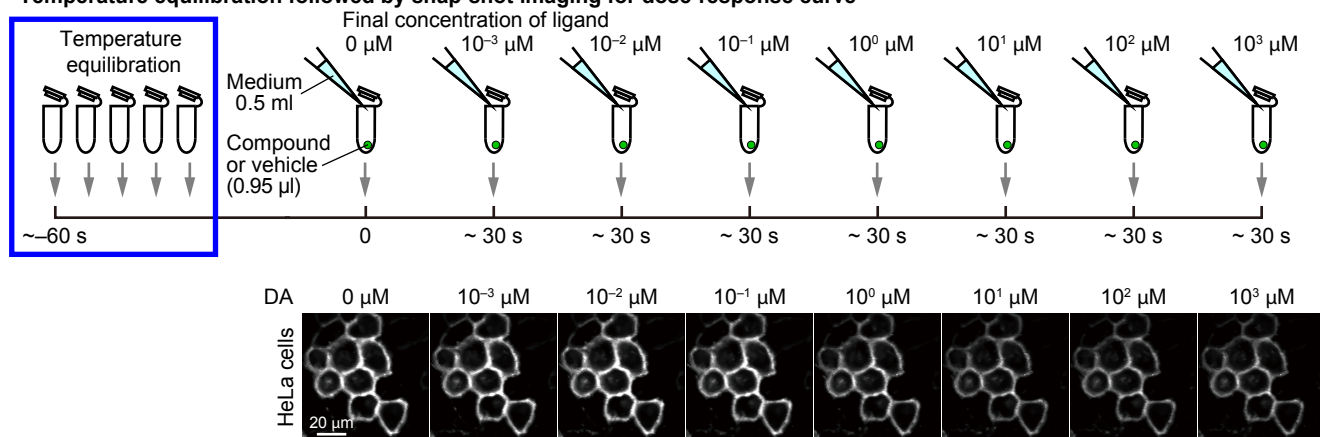
B Compound application for snapshot imaging



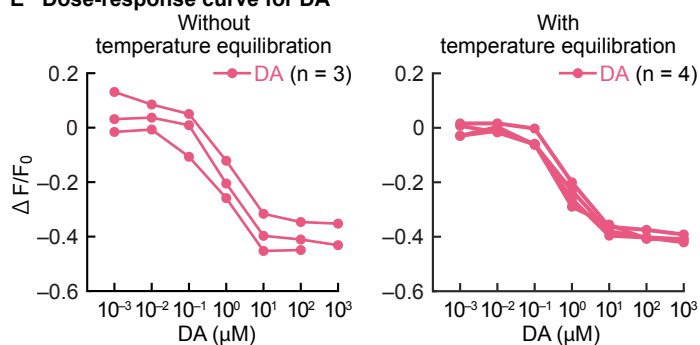
C Updated compound application for snapshot imaging



D Temperature equilibration followed by snap-shot imaging for dose-response curve



E Dose-response curve for DA



F Confirmation of R-GenGAR-DA1 stability

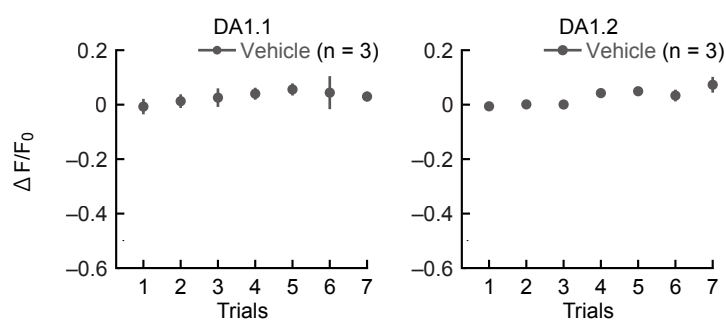
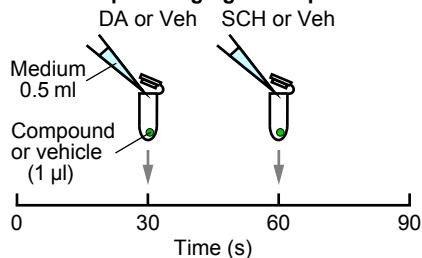
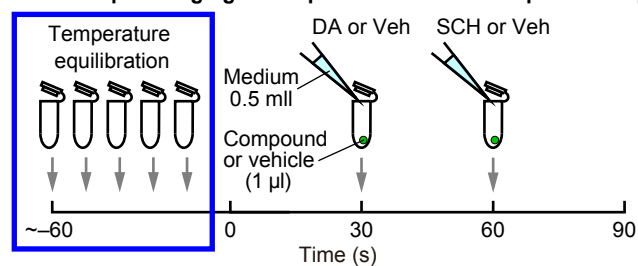


Figure S5

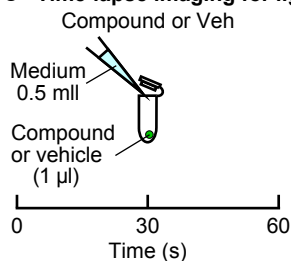
A Time-lapse imaging for response to DA (Fig. 1D, Fig. S1B and C, Fig. S2B, and Fig. S6C)



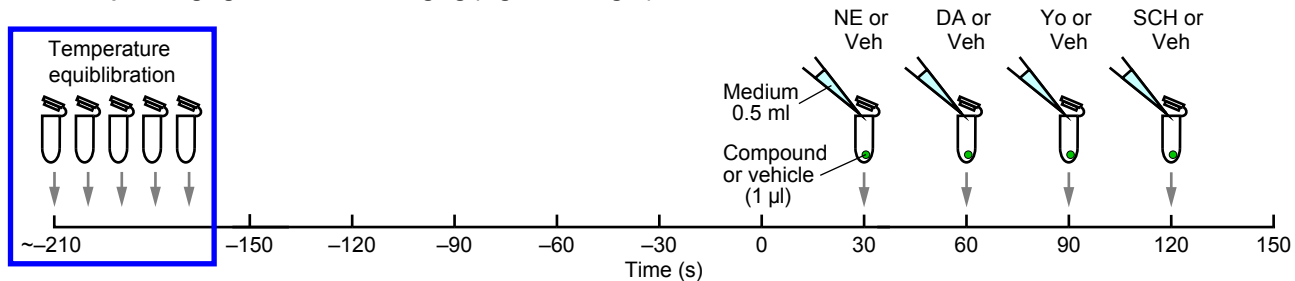
B Time-lapse imaging for response to DA with temperature equilibration (Fig. 2C, and Fig. 4B)



C Time-lapse imaging for ligand specificity (Fig. 2E)



D Time-lapse imaging for dual-color imaging (Fig. 3, and Fig. 5)



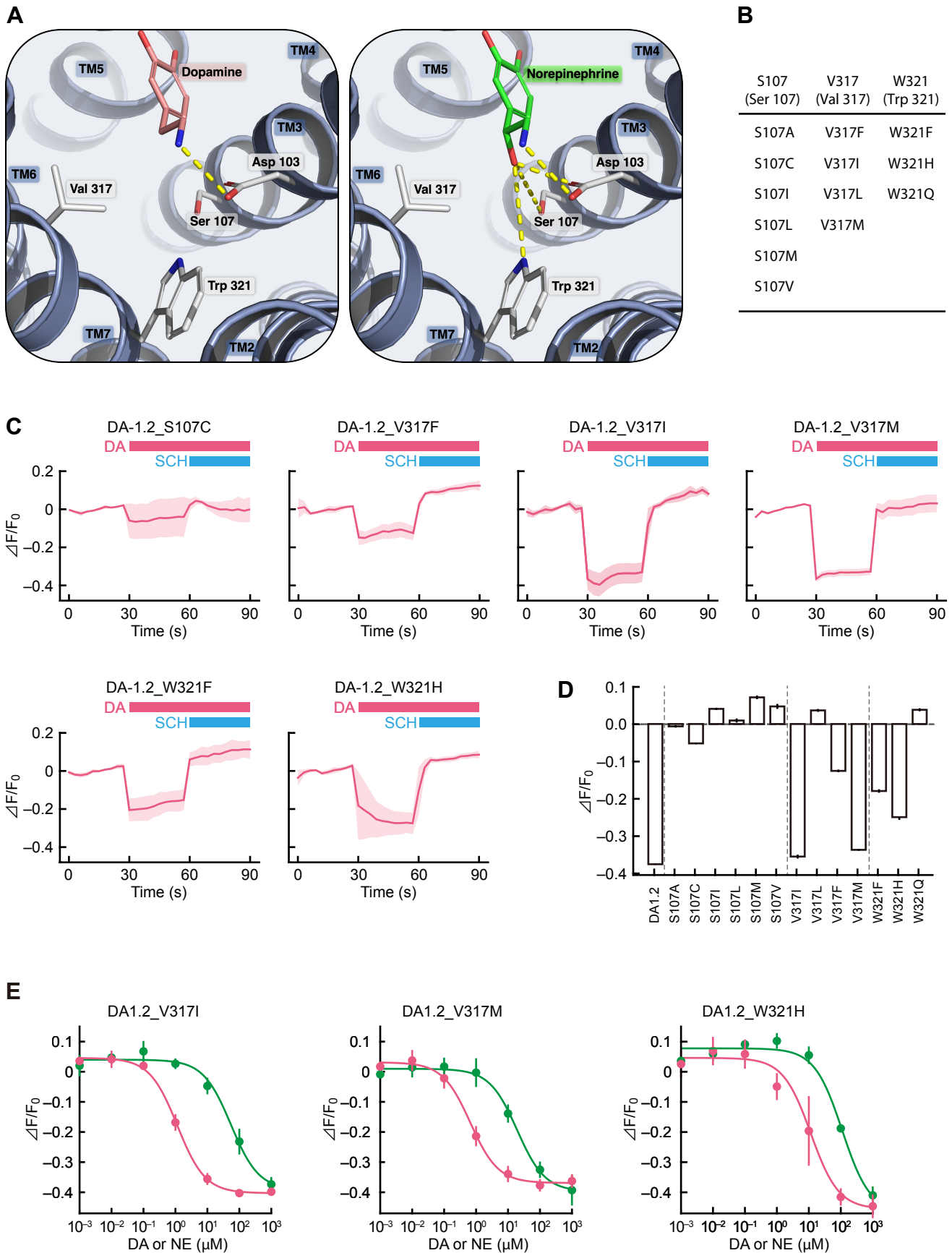


Figure S7

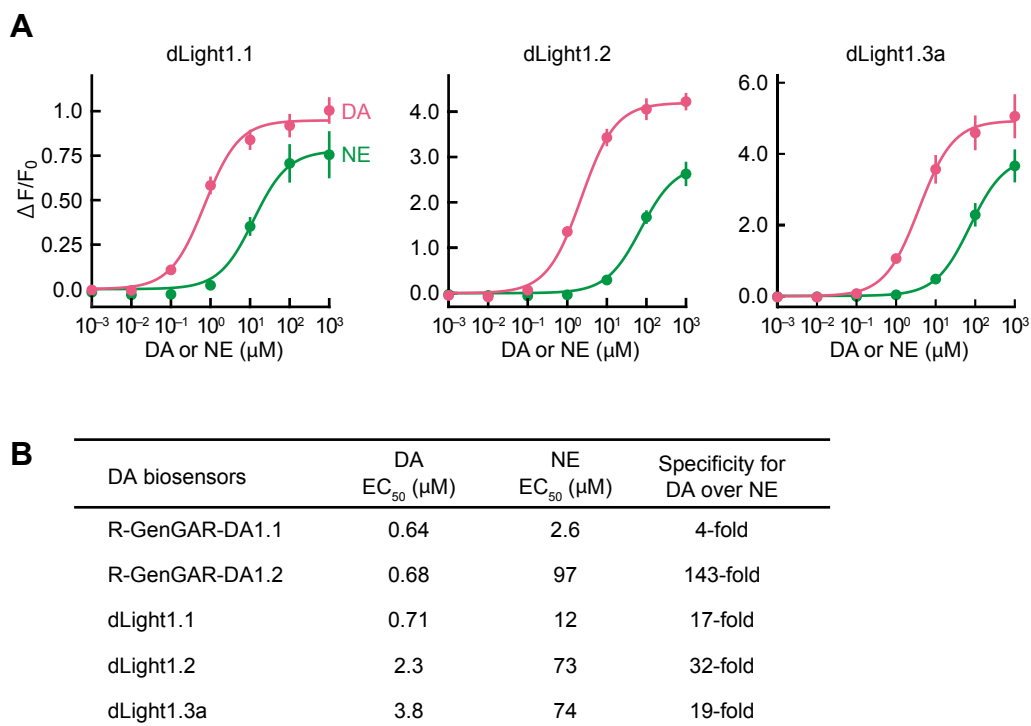


Figure S8

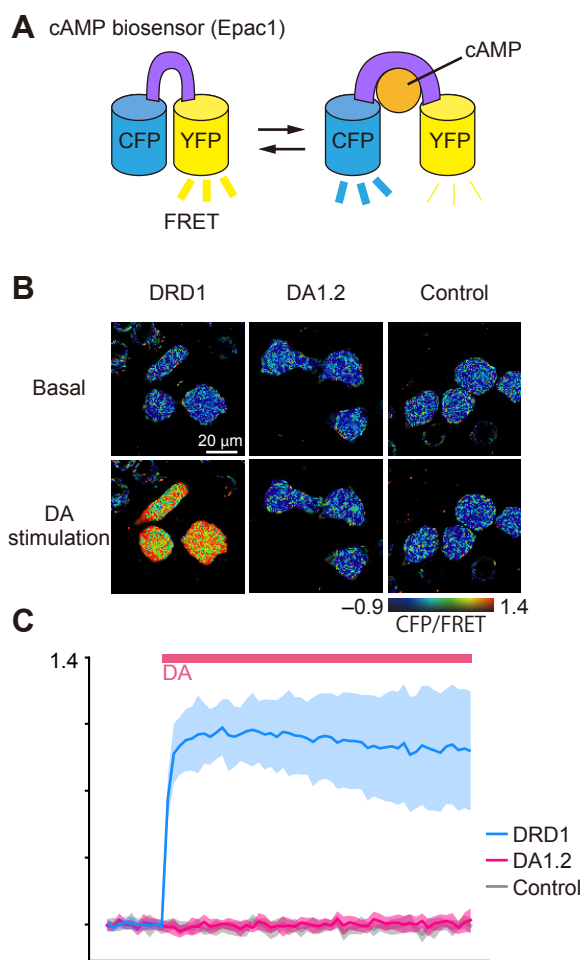


Figure S9

